Carbon 96 (2016) 285–302

Contents lists available at ScienceDirect

Carbon

journal homepage: www.elsevier.com/locate/carbon

In situ measurement of the strains within a mechanically loaded polygranular graphite

T.J. Marrow [a], D. Liu [b, *], S.M. Barhli [a], L. Saucedo Mora [a], Ye. Vertyagina [a], D.M. Collins [a], C. Reinhard [c], S. Kabra [d], P.E.J. Flewitt [b, f], D.J. Smith [e]

[a] Department of Materials, University of Oxford, UK
[b] Interface Analysis Centre, School of Physics, University of Bristol, UK
[c] Diamond Light Source, Harwell Science and Innovation Campus, Oxfordshire, UK
[d] ISIS Neutron Source, Rutherford Appleton Laboratory, Harwell Science and Innovation Campus, Oxfordshire, UK
[e] School of Engineering, University of Bristol, UK
[f] HH Wills Physics Laboratory, School of Physics, University of Bristol, UK

ARTICLE INFO

Article history:
Received 6 July 2015
Received in revised form
14 September 2015
Accepted 15 September 2015
Available online 18 September 2015

ABSTRACT

Neutron diffraction and synchrotron X-ray diffraction and imaging have been applied to study, in situ, the mechanical response to tensile and bending loading of polygranular Gilsocarbon nuclear grade near-isotropic graphite (grade IM1-24). Digital image correlation of X-ray radiographs and digital volume correlation of tomographs allow measurement of bulk elastic moduli and examination of the heterogeneity of deformation in the microstructure. Both the neutron and X-ray studies show the application of tensile strain reduces the bulk elastic modulus. A permanent set is observed to develop with applied tensile strain. The elastic strains within the graphite crystals were measured by diffraction; a cross-correlation analysis method has been applied for greater speed, robustness and improved precision in the measurement of the change in basal plane separation distance. In compression, a linear relation is observed between the elastic strains in the graphite crystals and the applied strain. In tension, this relationship is non-linear. The results are discussed with respect to the distribution of elastic and inelastic strain within the graphite microstructure. It is deduced that the significant residual elastic strains in the as-manufactured graphite are relaxed by microcracking as tensile strain is applied.

1. Introduction

In contrast to the naturally occurring mineral graphite [1], artificial polygranular graphite is a material that can be tailored to a wide range of applications. These include crucibles and components with high thermal shock resistance at elevated temperatures [2]; targets for particle accelerators [3]; various electrical and energy storage applications [4,5]; and even light-weight, high thermal conductivity engine pistons [6]. One significant use is in nuclear fission systems [7], where polygranular graphite must maintain its moderating, physical, and mechanical properties under a radiation environment even at high temperatures [8]. For nuclear applications, the graphite is typically manufactured from calcined cokes, re-impregnated with coal or petroleum pitches, so that after graphitization at temperatures in excess of 2500 °C the resulting heterogeneous microstructure comprises filler particles within a matrix containing ground filler “flour” and graphitized pitch. The overall material contains pores and flaws arising from manufacture. Early nuclear graphites had quite anisotropic properties due to the alignment of elongated ‘needle’ coke particles during moulding or extrusion [9]. A subsequently developed graphite, with near-isotropic structures and properties, is currently used in the UK Advanced Gas-cooled Reactors (AGR) [10] and graphite is a key structural material for advanced Generation IV nuclear fission reactors such as the VHTR (Very High Temperature Reactor) [11,12]. This paper examines the UK AGR graphite, which is a moulded isotropic coarse grained IM1-24 grade, made from Gilsocarbon filler particles (size ~500 μm) re-impregnated with a binder pitch [13]. Similar isotropic polygranular nuclear graphites can be coarse or fine grained. For example, the coarse grained H-451 (particle size ~ 500 μm [14]) is the reference material for the High-Temperature Gas-Cooled Reactor (HTGR or

* Corresponding author.
E-mail address: Dong.Liu@bristol.ac.uk (D. Liu).

http://dx.doi.org/10.1016/j.carbon.2015.09.058

VHTR) applications [15], while other graphites considered for high temperature fission reactors include the coarse grained NBG-18 [16] (particle size ~ 300 μm) and IG-110, which has a fine-grained (particle size ~ 25 μm) filler [17]: IG-11 is an unpurified grade of IG-110 [18,19].

The mechanical properties of non-irradiated polygranular nuclear graphite include non-linear elastic deformation and the development of permanent set after straining (e.g. Ref. [20]). The linearity of the elastic deformation, the magnitude of elastic modulus and the strength all increase with fast neutron irradiation [10]. Nuclear graphite also exhibits effects of size and stress state on strength [21]. For instance, specimens tested in bending usually fail at higher strains than tensile specimens, but the reason for the difference remains unresolved even after corrections are made for the non-linearity of the stress–strain curves [22]. In addition, size effects are not fully explained by Weibull-type approaches that consider the relative stressed volumes in the strain gradient (e.g. Ref. [23]). For safety-critical nuclear applications, there is a need for accurate prediction of structural graphite component strengths and their statistical variation [24]. This needs to be supported by a deeper understanding of how these complex graphites deform and fractures. Various approaches considering, for example, the length-scale of the heterogeneous microstructure [22] and weakest-link concepts have been developed that conservatively predict the failure strength of full-scale components from small test specimens, e.g. Refs. [15,24,25]. Their further development and experimental validation will require a detailed study of the processes of strain and damage development within the graphite microstructure.

It has been proposed that the mechanical properties of polygranular graphites are affected by internal strains within its microstructure. For instance, the permanent set that develops in polygranular graphite after the application of strain can be removed by thermal annealing [26], which has been suggested to relieve internal residual stresses. Complex patterns of residual elastic strains (i.e. residual stress), which arise from the significant anisotropy of the graphite crystals, are expected in as-manufactured nuclear graphite [27] as originally predicted by Mrozowski [28]. Their existence has recently been demonstrated in IM1-24 and NBG-18 graphite [29] by Raman spectroscopy, where a significant mean tensile strain was measured in the filler particles and a lower mean compressive strain in the surrounding matrix. The latter strains were higher in magnitude by factor of up to ~2–3 adjacent to cracks and pores. An increase in strength following pre-strain at high temperatures (~2500 °C) close to the graphitization temperature was observed in early studies [30] of a coarse-grained reactor grade graphite (H4LM grade, similar to IM1-24); this was deduced to relieve residual stress and also reduce the effects of the microcracking, which was expected to occur from the thermal strains of graphitisation. Relief of residual stress was also proposed as a contributing mechanism in studies of the effect of temperature on compressive and tensile strengths of coarse grained isotropic graphites that were similar to IM1-24 [31,32]. Further evidence, attributed to microcracking and strain accommodation by basal plane slip, comes from acoustic emissions [33,34], which have been observed to occur continuously during both compressive and tensile loading of IM1-24. The elastic modulus of nuclear graphite also changes with applied stress; compression tests of a graphite with a microstructure similar to IM1-24 reduced the elastic modulus [35]. The effect was attributed to localized cracking, which was judged to be finely dispersed since preloading in compression at high stresses had little effect on the tensile strength. Similar studies in the fine-grained IG-11 found a greater contribution from tensile pre-strain than compression, although both reduced the dynamic elastic modulus measured under load [36]. Mercury porosimetry of the pre-strained samples measured an increase in the pore content under tension and a decrease under compression. These effects were attributed to the larger number of microcracks formed due to tensile stress, with a secondary effect of plastic strain by basal slip. In summary, although it is well accepted that internal stresses and local deformation processes such as microcracking occur and that these affect the bulk properties of graphite, there have been few reported experiments that evaluate either the stresses and strains within graphite, or their development during loading.

Polygranular graphite is treated as a linear elastic material in engineering design; its structural integrity may be conservatively assessed using either linear elastic fracture mechanics [14,37] or more advanced developments such as strain energy density [38] and continuum mechanics [39]. Nuclear graphite is, however, a heterogeneous quasi-brittle material. For both coarse and fine grained non-irradiated isotropic graphite there is non-linear elastic behaviour (as discussed above), a rising fracture resistance curve with crack propagation (J–R curve) [40–43], and also the development of a micro-cracked fracture process zone [44–46] that has been observed in NBG-18 and IM1-24, for instance. The strength of nuclear graphite, particularly in small test specimens, is quite sensitive to microstructure; in situ observations show that damage initiates from the larger porosity [20,21,47]. The microstructure, particularly the distribution of porosity, affects the crack path [44,48] and also the development of the microcracked fracture process zone [49,50]. Such microcracked fracture process zones are common to quasi-brittle materials as diverse as high toughness monolithic and composite ceramics [51], polymeric [52] and natural biological composites [53], geological minerals [54]and even volcanic structures [55]. The fracture process zone is a key factor in the size effect of strength [56]. For instance, small test specimens from nuclear graphite, which are extracted either from operating reactors or used in a material test reactor (MTR) accelerated experiments, provide data that may be used to predict the performance of structural components [57–59]. Whilst the magnitude of non-linear effects will be reduced in irradiated graphite, the need for high confidence in the margin of safety provided by such structural integrity assessments is a strong impetus for the development of non-linear elastic fracture mechanics models, for which the tensile behaviour of the material in the fracture process zone is fundamental [60–62]. Experimental methods that study damage development under tension are thus important to a wide range of problems.

Strain measurement by the two-dimensional digital image correlation (DIC) technique has been used for quantitative in situ studies of damage nucleation and propagation in a range of materials [63,64]. The measured displacement field, which can be obtained with high precision, is readily converted into a strain field. DIC, however, is confined to the surface of specimens. Measurements of the displacement field within a material by the three-dimensional digital volume correlation (DVC) technique, applied to high resolution computed tomography [65–67], can provide quantitative information of the processes of damage development and the strains within materials [68]. Image correlation measures total strains, and to study the elastic strains it is necessary to apply scattering techniques such as diffraction. Although widely applied to monolithic materials (e.g. Refs. [69–71]), the structures of heterogeneous materials (such as graphite) present difficulties due to load partitioning and interphase strains [72–74], which can give a complex relation between the applied stress and measured elastic strains.

The low attenuation by graphite of both high energy X-rays and neutrons allows the observation, by diffraction, of the strains within bulk samples. In this study, both have been used to assess

their relative precision and to validate independently the relation between the applied deformation and the elastic strains. X-rays also are well suited to total strain measurement by image correlation of high-resolution radiographs and tomographs in graphite [46]. Certainly the brightness of synchrotron radiation enables in situ studies with the necessary short times needed to capture images. Neutron imaging has low spatial resolution, and so was not used for similar work.

The objective of this work, which supports ongoing studies of the damage developed at stress concentrations and propagating cracks [45,46], is to better understand how the microstructure of a coarse grained polygranular graphite accommodates applied strain, and the effect of this applied strain on its mechanical properties. The relation between applied strain and residual inelastic deformation, and the difference in behaviour under tension and compression, are of particular interest. To study this, it is necessary to be able to observe, in situ, the relationship between the applied strains, the total strains in the microstructure of the material and the elastic strains in the crystals.

2. Experimental

2.1. Material

The material, supplied by EDF Energy, is a moulded IM1-24 Gilsocarbon (GCMB grade) polygranular nuclear graphite, manufactured by Graftech (formally UCAR), which has weakly-anisotropic properties. Depending on orientation, the elastic Young's modulus is reported to be between approximately 11.6 and 11.9 GPa, with a Poisson ratio of 0.2 and a tensile strength between 19 and 20 MPa at a strain of approximately 2500 με [75]. It is one of the graphite grades used in the core of the UK Advanced Gas-cooled Reactor fleet. The same grade, from different billets, has been studied in previous work by the authors [45,46,76]. All the specimens in this work were obtained from the same billet.

2.2. Synchrotron X-ray: tensile loading

The experiment to study tensile behaviour was conducted at the Joint Engineering, Environmental and Processing (JEEP – I12) imaging beamline at the Diamond Light Source in the UK [77], using a mono-chromatic X-ray beam energy of 80 keV. The test specimen (ASTM C565 geometry [78] with diameter 6.3 mm and gauge length 44.4 mm, Fig. 1a) was mounted vertically within a loading rig. A tensile load was applied under displacement control via a computer controlled stepper motor, with the balancing compressive load taken by an external polycarbonate tube (diameter 65 mm, thickness 10 mm). The specimen alignment was aided by a spherical bearing at each end of the load train. Several tungsten carbide balls (~0.25 mm dia.) provided fixed fiducial markers on the specimen surface to allow adjustments of the field of view during the experiment to accommodate vertical specimen movements under load. The balls were fixed using a small amount of cyanoacrylate adhesive, applied with a needle tip.

X-ray diffraction patterns were recorded using a Thales Pixium RF4343 42 cm × 42 cm detector (2880 × 2881 pixels, 16 bit depth), located at a distance of 2.55 m from the specimen. Ceria powder was used to calibrate the detector distance from the rotation axis of the specimen stage. Radiographs were recorded using a PCO.4000 CCD camera (4008 × 2672 pixels, 16 bit depth), with optics selected to image 7.2 × 3.2 mm (*'module 3'*, pixel size 1.8 μm) or 16 × 11 mm (*'module 2'*, pixel size 4.8 μm); the specimen to camera distance for imaging was 35 cm. Slits reduced the incident X-ray beam to a size of 1.5 × 1.5 mm for the diffraction observations. The slits were removed for radiography and tomography and the exposure time, both for diffraction and radiography, was 1 s. Computer scripts were used to control the experiment, in particular automating the changeover between imaging and diffraction modes that required around 30 s. Tomography was performed with 3600 radiographs over a 180° rotation using module 3; a standard back-filtered projection algorithm was used for the image reconstructions [79]. The obtained data is essentially a three-dimensional map of the X-ray attenuation of the microstructure.

The diffraction data sets were images of the diffraction rings up to a Bragg diffraction angle (2θ) of approximately 5.5°, which measure the separation, $d_{hk.l}$, of the diffracting planes in the crystal. The basal plane ring, denoted using hexagonal Miller-Bravais indices as *(00.2)*, occurs at 2.55° and has the highest expected intensity. The $d_{00.2}$ ring was the only ring analysed since the basal plane elastic modulus is the lowest in the graphite crystal by a significant factor [80]. The crystal anisotropic elastic moduli of graphite vary between 36 GPa, perpendicular to the basal plane, to 1060 GPa within the plane, due to the weak van der Waals forces between the basal planes. Data averaging by binning was performed after fitting an ellipse to find the ring centre for the $d_{00.2}$ diffraction peak. To achieve this, the image was divided into radial sectors at 1° bin intervals of the azimuth angle, and a radial intensity profile for each sector was obtained by integration [81]. In the conventional method of analysis, the intensity profiles are fitted with a Gaussian or pseudo-Voigt peak to identify the peak positions; the diffraction angle (2θ) is the distance between the ring centre and the peak, and the change in this is used to calculate the strain [82]. However, in this work a cross-correlation data analysis method was implemented to evaluate the peak shift and hence to improve the precision of strain measurement, which was assessed to have an uncertainty of approximately 12 με [See Appendix for details of this method]. Notably, this method provided measurements of peak shifts independent of diffraction line profile shape. This was deemed to be important for these data, which displayed broadened line profiles affected by the specimen geometry. Such broadened profiles would not be well determined by a pseudo-Voigt or a similarly analytic fitting function, without resorting to more complex convolution operations. The reference radial intensity profile (i.e. with a small pre-load of 10 N) of the $d_{00.2}$ peak was compared with the radial intensity profile under load to obtain the peak shift in both the vertical (axial strain, 0° azimuth) and horizontal (transverse strain, 90° azimuth) directions.

The intrinsic measurement error was evaluated by retrieving the relative $d_{00.2}$ change of pairs of diffraction patterns, between which the specimen had been translated several millimetres, rotated 90° and then returned to its original location and orientation, without a change in load. Three repeated measurements at two different locations in two orientations gave a standard error of 0.0092 pixels for the apparent change in ring radius, equivalent to a change in $d_{00.2}$ of 4.9×10^{-5} Å (one ångström or 1 Å is 0.1 nm). The strain measurement error is thus 14 με, which is consistent with the expected uncertainty (see Appendix).

Movements perpendicular to the detector have a geometric magnifying/diminutive effect; specimen displacement was corrected by direct measurement via digital image correlation (DIC) of radiographs. These measurements were acquired before, or after, each set of diffraction observations with the specimen at the same load and rotated at 90°. The multi-pass DIC analysis used the LaVision StrainMaster DaVis software (Version 7.2) with decreasing subsets of 512 × 512 pixels (2 passes) and 256 × 256 pixels (3 passes), both at an overlap of 50%. A DIC assessment of radiographs recorded with a controlled displacement obtained a standard error of 0.8 μm, so that the corresponding uncertainty in the correction of the shift in $d_{00.2}$ was 10^{-6} Å, i.e. an insignificant strain error of approximately 0.3 με. The movements increase in magnitude with

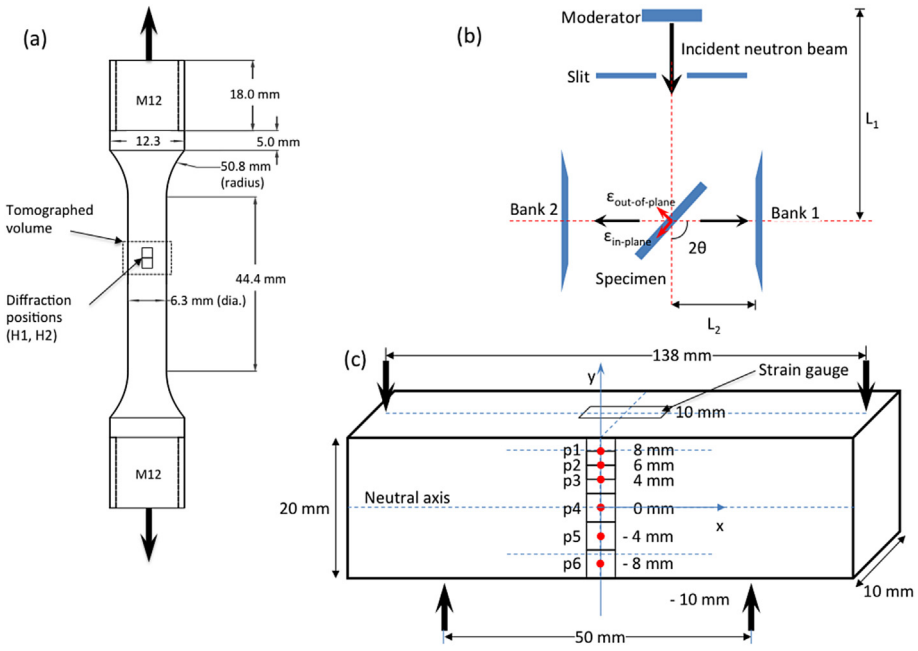

Fig. 1. Schematics of a) tensile specimen, indicating positions of X-ray diffration measurements (H1 & H2) and tomography; b) neutron beamline arrangement of four-point bending specimen and time of flight detector banks; c) bend specimen, indicating positions of strain gauge and neutron diffraction measurement positions (p1–p6). (A colour version of this figure can be viewed online.)

the applied load, and were measured to be up to 200 μm. Without correction these would have introduced errors in $d_{00.2}$ of up to 2.7×10^{-4} Å (i.e. a strain error of approximately 80 με).

The tensile load was slowly varied by cycling the applied displacement, with a progressive increase in the peak load of approximately 50 N (i.e. 10%, 20%, 30% etc. of the nominal failure load of approximately 500 N, which had been measured in preliminary tests); failure occurred at 505 N (i.e. at a stress of 15.8 MPa). Within each cycle, the load was increased in about 5 stages to the chosen peak and the specimen was unloaded in similar stages to approximately 20 N. At each stage, diffraction patterns were collected in each of two locations that were separated in height by approximately 2 mm (marked as H1 and H2 in Fig. 1a). At the selected positions, data were obtained in two orthogonal directions via specimen rotations of 90°. Radiographs were obtained too, using the *'module 3'* (pixel size 1.8 μm) optics in two orthogonal orientations at the peak load and unloaded at the end of each cycle, and with the *'module 2'* (pixel size 4.8 μm) optics in one orientation. Tomographs were recorded at the preload of 10 N and at 50% of the expected failure load, and the volume sampled is shown in Fig. 1a.

2.3. Neutron diffraction: bending loading

The experiment to study behaviour in four-point bending was conducted at ENGIN-X, which is a time of flight (TOF) neutron diffractometer at the Rutherford Laboratory in the UK. The diffractometer is a high resolution instrument optimized for strain studies and has a high neutron flux over the 1 to 4 Å wavelength range [83]. The primary flight path for the neutron beam (L_1) is ~50 m and the secondary flight path (L_2) is ~1.53 m. This corresponds to the distance between the centroid of the instrumental gauge volume (IGV) within of the specimen and the banks of detectors. A 4 × 4 × 4 mm IGV was selected to optimize count times with an acquisition time per measurement position of 20 min. ENGIN-X has two detector banks that are centered about the IGV and at $2\theta = 90°$ to the incident beam (Fig. 1b). Bank 1 provides TOF data along the length of the specimen (i.e. the in-plane strain), whereas Bank 2 provides the out-of-plane strain. The plane in this case is defined as that in which the bending takes place.

The TOF spectra recorded by the detectors in each bank are transformed into a common inter-plane spacing scale to obtain the diffraction spectrum [84]. Standard calibrations were performed with a Ceria powder sample. Conventionally, the Bragg diffraction peak position is obtained by a least squares refinement fit of a pseudo-Voigt function convolved with a leading and trailing exponential function (accounting for the inherent asymmetric diffraction line profiles of the neutron diffraction data) to allow the crystal strain to be measured from the relative change in peak position. For consistency with the X-ray diffraction analysis, only the $d_{00.2}$ peak for Bank 1 was considered using the same correlation-based method to determine the shifts with applied load. Initial spectra recorded at each position of the IGV in the free-standing condition provided the reference. A comparison between the conventional and correlation-based methods is given in the Appendix. The expected error of the neutron strain measurements is 50 με [85].

The test specimen, a rectangular graphite beam (10 × 20 × 150 mm length), was subject to four-point loading (outer span 138 mm, inner span 50 mm). Neutron diffraction measurements were obtained at six locations **p1** to **p6**, as shown in Fig. 1c, where **p1** and **p6** are 8 mm from the neutral axis. The flexure rig applies load via a finely-threaded bolt and has no direct load measurement, so strain gauges with a measurement area of 2.5 × 4 mm were attached to the upper and lower surfaces of the specimen to monitor the longitudinal surface strains. Tests of several identical specimens of the same graphite, performed with the addition of strain gauges attached to the cross-section, verified the linear variation of strain, and also the symmetry of the tensile and compressive surface strains measured at a distance of 10 mm from the neutral axis. The surface strain gauges remained stable to better than 5 με over the 2 h period of each neutron data acquisition. The applied in-plane strains at the IGV locations could then be obtained by linear interpolation between these surface strain gauge measurements.

The flexure load was incrementally cycled by adjustment of the

bolt and the response was monitored using the surface strain gauges to attain peak strains of approximately 900, 1500 and 1800 με. Up to eight observations were made in each cycle as the load was increased in stages, and then decreased again to the unloaded state. In the fourth and final cycle, the specimen was loaded to failure in stages of approximately 200–500 με. The final fracture propagated from the tensile surface at a strain of ~3200 με.

3. Results

3.1. Material microstructure

A section of the three-dimensional microstructure, observed by computed tomography, is shown in Fig. 2. This example illustrates the characteristic coarse ellipsoidal Gilsocarbon filler particles, with a typical size of up to approximately 1 mm, within a matrix of graphitized pitch and finer 'flour' particles produced by the grinding of larger filler particles during manufacture. Porosity, which is in dark contrast due to the lower X-ray attenuation, exists on a wide range of length scales from around 0.5 mm down to below the resolution limit of a few μm. However, the microstructure of this grade of graphite contains pores down to the nanometre length [13,86]. The large pores play an important role in the nucleation of fracture [46,87]. The small bright, highly attenuating, regions are probably due to concentrations of metallic impurities such as Iron that remain after graphite manufacture [88], although phase contrast from the edges of pores will have similar appearance and is also a possible cause, as a phase retrieval algorithm was not used in the tomographic reconstruction of these data. The orientation of the sample relative to the axis of the original billet is not known, nor is it apparent from visual examination of the microstructure.

3.2. Synchrotron X-ray: tensile loading

Maps of the vertical axial strain obtained in each cycle are presented in Fig. 3a, at the peak load, and in Fig. 3b after unloading.

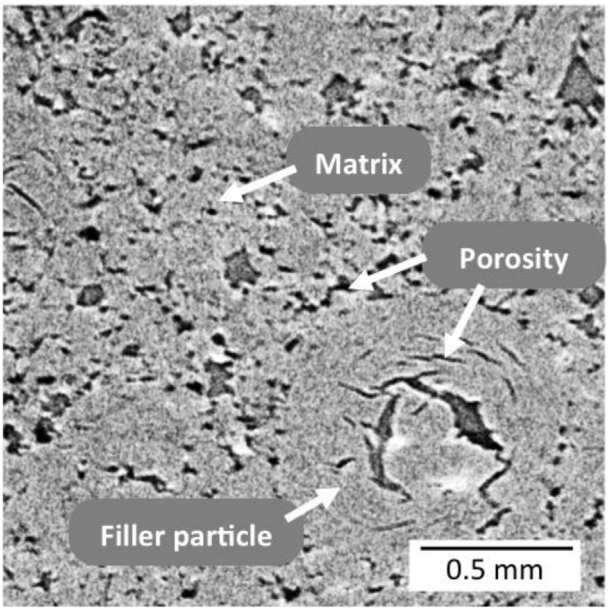

Fig. 2. A 2D slice of a tomographic image of the Gilsocarbon GCMB UCAR microstructure, showing the characteristic coarse filler particles within a matrix of graphitized pitch and finer (ground) filler particles. Pores are visualized as dark regions of low X-ray attenuation.

This strain was measured by digital image correlation of the radiographs, where the contrast is due to the graphite porosity that provides the necessary 'speckle' for image correlation (an example radiograph is shown in the bottom right image of Fig. 3b). The strains were measured with respect to a reference radiograph recorded at the start of the experiment at a small preload of 10 N. The multipass DIC analysis used a decreasing subset size of 512 × 512 pixels (2 passes) and 256 × 256 pixels (3 passes), both with an overlap of the 50%. The displacement fields were corrected for rigid body movement and rotation by finding the rotation centre and angle that minimized the standard deviation of the displacement field. A typical rotation was centred approximately 35 cm above the field of view (i.e. close to the top of the loading rig), with a rotation angle of 0.03°. The axial strain is visualized as the gradient of the vertical component of the displacement field; the strain maps in Fig. 3 were those obtained with the specimen in the 90° rotation position. The positions of the diffraction measurements (H1 and H2), defined by the slits, are marked by solid line boxes and the tungsten carbide fiducial balls, seen in the reference radiograph (Fig. 3b, bottom right), were masked in the DIC analysis. The strain maps in Fig. 3a show, qualitatively, a progressive increase in the axial strain in the loaded state. The patterns of strain are heterogeneous, and remain similar in distribution as their magnitude increases. The corresponding strain maps obtained in the unloaded state (Fig. 3b) show a similar pattern of residual heterogeneous strains to the loaded state, which also increase in magnitude as the peak initial applied load increased.

The average strains in the imaged region were obtained directly from the displacement field, and will be referred to in this paper as the *bulk strains*, for convenience. The net displacements were calculated between sets of opposing points, (i) to (vii), across the observed field, which are numbered on the radiograph in Fig. 3b. These provide measurements in the vertical and horizontal directions across the region that is indicated by a dotted box in each strain map. The average strain was calculated simply as the displacement difference relative to the separation between the measurement points, which was approximately 2.5 mm. The average bulk axial strains during loading and unloading, as a function of the applied tensile stress, are presented in Fig. 4. The error bars show the standard deviation, and the apparent hysteresis in each load cycle is within the measurement uncertainty. The bulk axial tensile strain increases linearly with stress in each cycle (Table 1). Data were obtained similarly from module 3 radiographs recorded in the 0° rotation direction and also from the module 2 radiographs, which had a measurement point separation (i.e. gauge length) of approximately 5 mm. The elastic moduli, which were measured as a linear fit to the stress/strain plot during unloading (to avoid the effect of non-linearity with loading), are also reported in Table 1, and these show a tendency to decrease with increasing peak stress. Interestingly, the moduli obtained from the longer gauge length measurements are more scattered than those measured over the shorter gauge length; the latter always fall within the uncertainty margins of the former.

The strain measurements between each of the seven opposing points are presented individually in Fig. 5, both at the peak of each cycle and after unloading. There is a progressive increase in the axial and transverse bulk strains at the peak of each successive load cycle (the error bars are calculated from the DIC displacement uncertainty). Failure occurred during cycle 7; the data presented for this final cycle were obtained after failure, and are significantly more localised than the previous cycles. The unloaded axial strains vary consistently across the specimen, being tensile towards one side and compressive to the other (Fig. 5b). The transverse strains show similar behaviour to the axial strains, with compressive transverse strains corresponding to tensile axial strains and vice

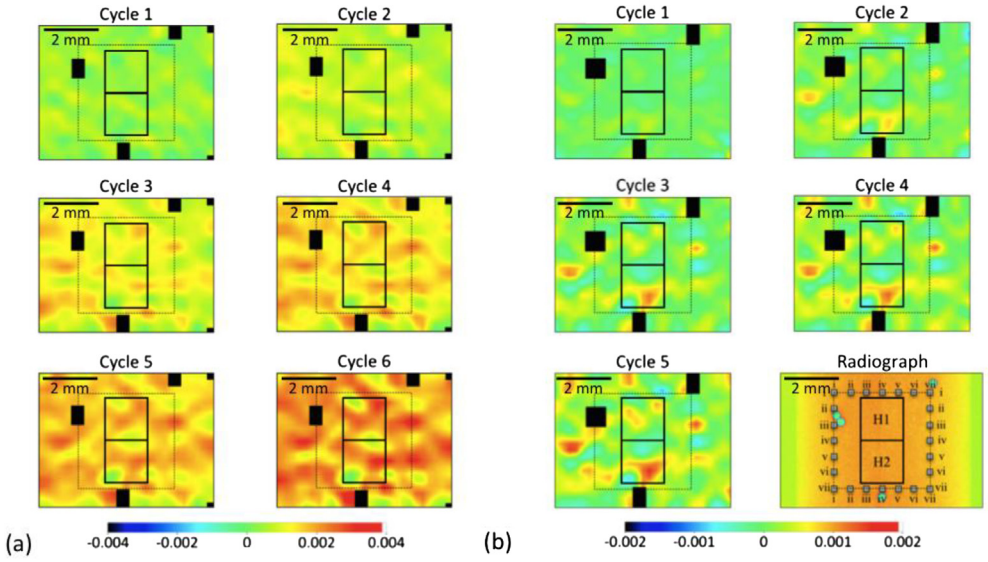

Fig. 3. Axial strain maps obtained by image correlation of X-ray radiographs of the tensile specimen; a) at the peak applied stress in cycles 1–6, and b) after unloading from the peak stress in cycles 1–5. The radiograph presented in the bottom right image shows the fiducial marker balls, and indicates the diffraction locations H1 & H2 and the measurement points, (i)–(vii) for the average strain calculation. The fiducial balls are masked (black zones) in the strain maps. The data are at location H1 in the 90° orientation. (A colour version of this figure can be viewed online.)

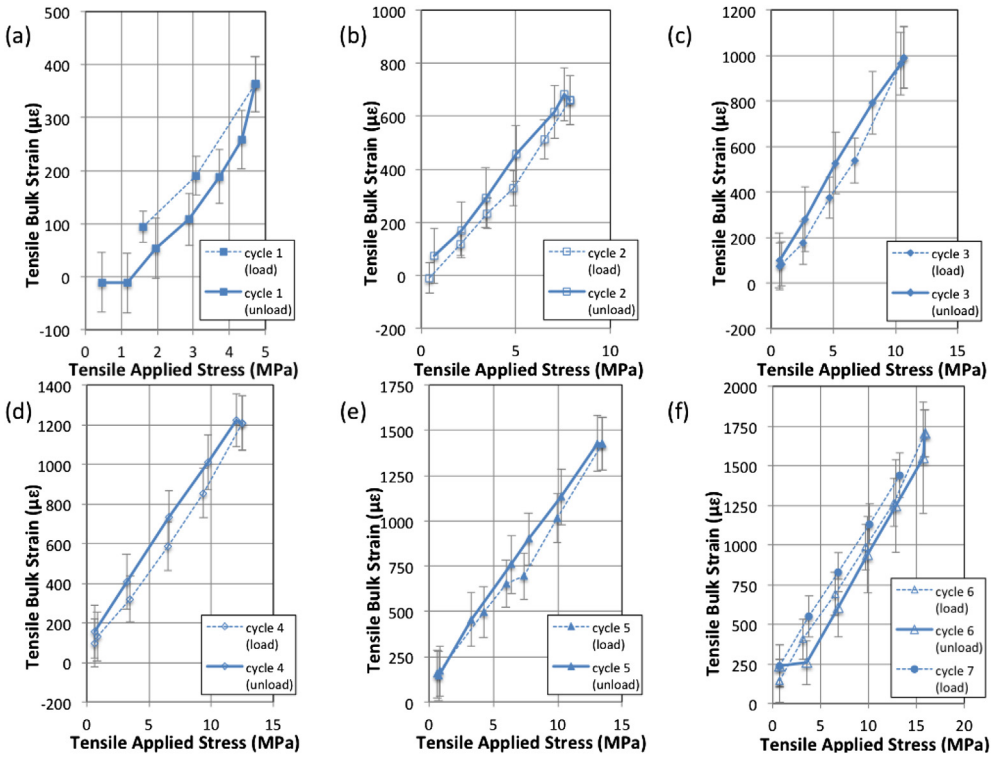

Fig. 4. The axial average bulk strains in the tensile specimen, measured using image correlation of radiographs (module 3), as a function of the tensile applied stress. Data for cycles 1–7 are presented for location H1 in the 90° orientation, with a displacement measurement gauge length of 2.48 mm. The error bars are the standard deviation of the measurements, (i)–(vii), in each case. Failure occurred in cycle 7. (A colour version of this figure can be viewed online.)

versa. The ratio of the average transverse bulk strain to the average axial bulk strain remains approximately constant as the load is increased (Fig. 6), with consistent data obtained in both the 0° and 90° rotations. A linear fit provides a Poisson's ratio of 0.20 ± 0.03, which is in good agreement with independent measurements [75]. The two outlying data points are from the highest strains measured in cycle 7 after failure. The ratio of transverse to axial bulk strains in the unloaded state (Fig. 6b) is scattered due to the small values of transverse strain, and shows no obvious trend. Similarly, there is no clear trend between the local values of transverse strain obtained under load and after unloading (Fig. 6c).

A volume of the reconstructed tomograph is shown in Fig. 7a; the lighter horizontal bands are a 'streak' artifacts from the highly attenuating tungsten carbide fiducial balls. These move together

Table 1
Tensile experiment data for peak stress, strain and elastic modulus at location H1 in the 90° rotation, measured by image correlation with module 3 images (2.48 mm gauge length), and elastic modulus measured similarly with module 2 images (4.97 mm gauge length) at the same location. The moduli are measured by a linear fit to the stress and strain data during unloading only.

Cycle	Peak applied tensile stress (MPa)	Peak tensile strain (με) (Gauge length 2.48 mm)	Elastic modulus (GPa) (Gauge length 2.48 mm)	Elastic modulus (GPa) (Gauge length 4.97 mm)
1	4.23	380 ± 120	11.95 ± 0.78	14.94 ± 5.68
2	7.52	790 ± 70	11.19 ± 0.32	9.94 ± 2.66
3	10.47	1140 ± 70	11.07 ± 0.26	8.98 ± 1.63
4	12.25	1430 ± 100	10.71 ± 0.12	9.17 ± 1.21
5	12.99	1630 ± 70	9.75 ± 0.21	9.35 ± 1.04
6	15.68	1960 ± 160	10.45 ± 0.86	–

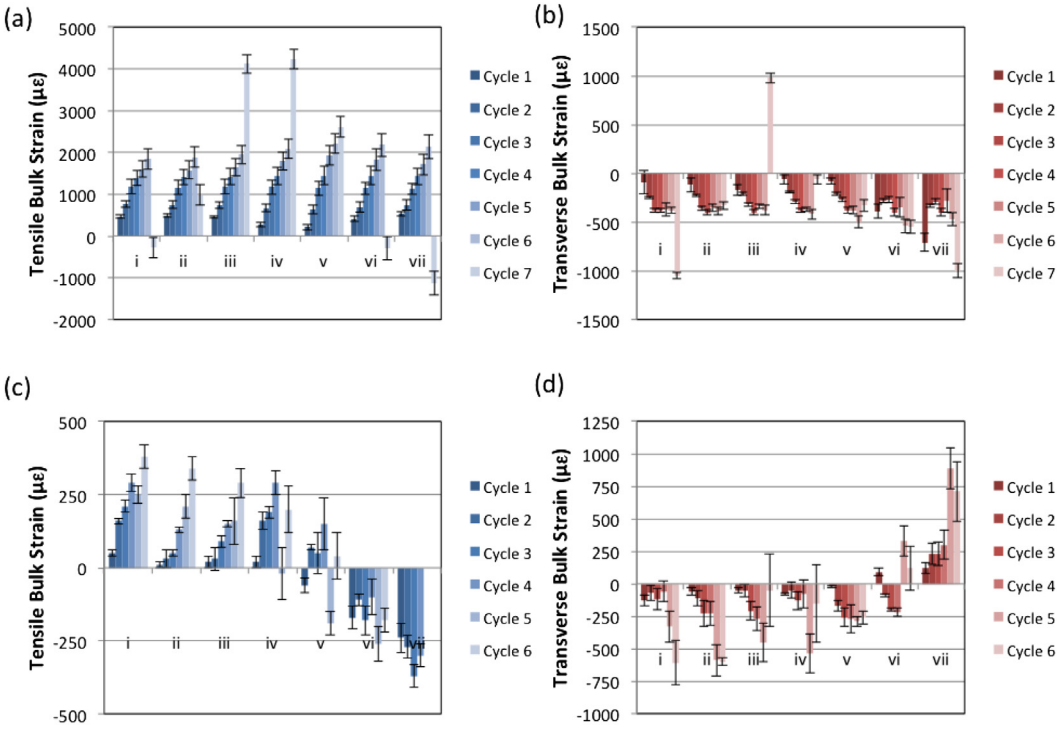

Fig. 5. The variation of axial and transverse strains across the gauge area, measured by image correlation of radiographs (module 3) for the 90° rotation at location H1 in the tensile specimen. The strains under load are presented in (a) for axial tensile strain and b) transverse strain. The corresponding strains after unloading are presented in (c) and (d). The measurement locations, (i) to (vii) are indicated in Fig. 3b (bottom right). The error bars are obtained from the image correlation measurement uncertainty (one standard deviation). Note the differences in scale of the vertical strain axes. (A colour version of this figure can be viewed online.)

with the specimen, and had no measurable effect on the digital volume correlation (DVC) analysis, which was performed with the LaVision DaVis software (Version 8) using the following parameters: 2 passes with an interrogation subset of 256 × 256 × 256 voxels at 50% overlap, followed by 3 passes at 75% overlap with a 128 × 128 × 128 voxel subset. As with the radiographs, the porosity of the microstructure provides the necessary 'speckle' for the image correlation. The reference tomograph was recorded at a tensile load of 10 N, and was correlated with the tomograph obtained at a tensile load of 250 N, i.e. at a stress of approximately 7.5 MPa. After removal from the obtained displacement field of the rigid body translations and small rotations (of approximately 0.02°), using the methods described in Ref. [89], the axial strains were calculated from the relative change in displacement across the volume (Fig. 7b). The obtained average axial bulk strain of 727 με is consistent with the radiograph data (i.e. Fig. 4); there is a total variation of about 60 με across the volume, which is comparable to that observed in the analysis of the radiographs (Fig. 5). The average gradient of the strain variation in Fig. 7c is 40 με/mm in a direction intermediate between the *x* and *y*-axes (obtained by fitting a plane to the data). The transverse strains were examined in the same manner, but were too small to be measured with sufficient reliability to extract the Poisson's ratio.

To examine local variations in strain, sub-volumes that individually surrounded 55 filler particles and 25 matrix regions of different sizes were extracted from the tomographs. The filler particles ranged in size from ~0.1 mm^3 to 4.4 mm^3 and the matrix volumes varied from 0.2 to 1.1 mm^3. Digital volume correlation analysis of the extracted sub-volumes, to measure the relative deformation with 7.5 MPa tensile applied stress, was performed with the following parameters: a 32 × 32 × 32 voxel interrogation subset, with 75% overlap and two passes, followed by a 16 × 16 × 16 interrogation subset, with 75% overlap and three passes. For the filler particles, the considered displacement vectors were only those contained inside an ellipsoid that was defined manually by inspection of the characteristic "onion-like" porosity of the filler particle; this is illustrated in Fig. 7c, in which pores and solid graphite have been segmented via their X-ray attenuation using a simple threshold criteria. The axial strain was calculated for each sub-volume as the vertical gradient of the average axial displacements of each horizontal plane (Fig. 7d). Comparison of the axial strains for the filler particles and matrix (Fig. 8a) shows significant

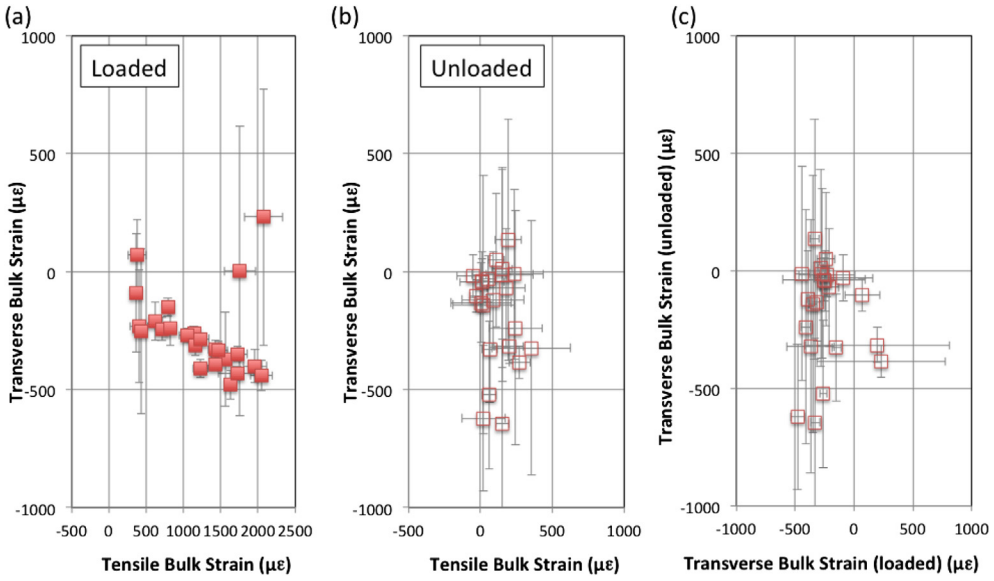

Fig. 6. The relationship between average axial bulk strain and transverse strain for the tensile specimen, measured by image correlation of radiographs (module 3). Data are combined for locations H1 & H2, and the 0° & 90° orientations. Data shown for the specimen in the a) loaded and b) unloaded state. A comparison of the transverse strains, measured in the loaded and unloaded states, is shown in c). The error bars are one standard deviation of the measurements, (i)–(vii), in each case. (A colour version of this figure can be viewed online.)

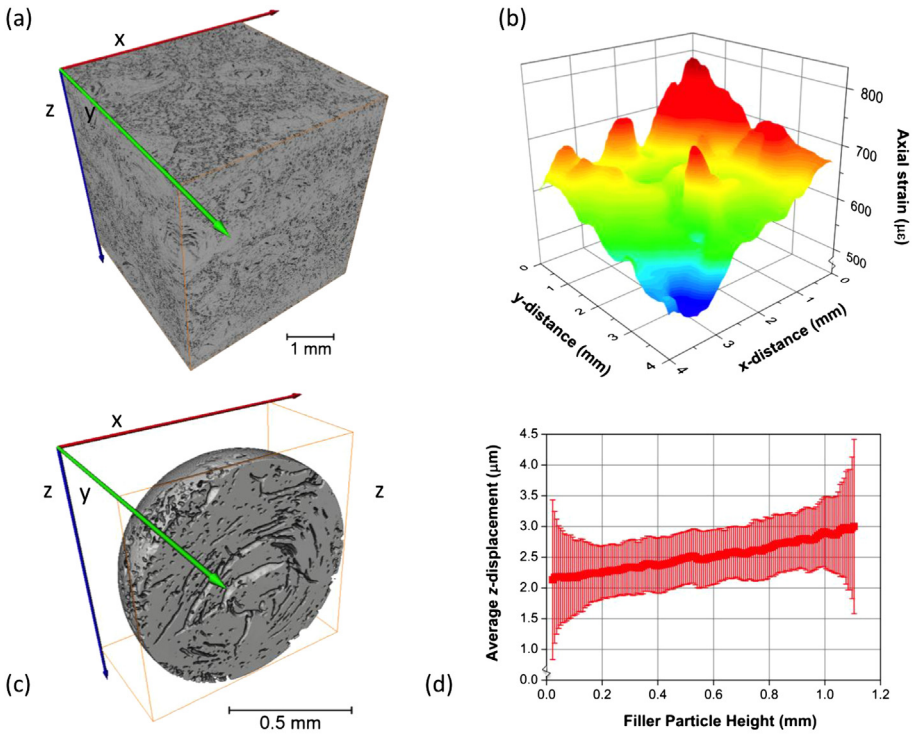

Fig. 7. X-ray computed tomography of the tensile specimen; a) cropped volume (4.32 × 4.32 × 4.68 mm), visualized as attenuation map (low attenuation is dark); b) axial strain, mapped using the image correlation measured displacement difference across the cropped volume between the preloaded state (10 N) and loaded state (250 N, ~7.5 MPa tensile stress); c) visualization of the pores in a filler particle (diameter ~ 1.1 mm); d) slice-by-slice variation of average vertical (z) displacement across the filler particle, measured by image correlation. The error bars are one standard deviation for each slice. The z-axis is parallel to the vertical tensile direction. (A colour version of this figure can be viewed online.)

scatter about the bulk average strain, with a tendency for higher strains to develop in the matrix. Although the local strains do vary systematically with position (Fig. 8b–d), the scatter of strain was predominantly due to heterogeneity in the microstructure, particularly from the filler particles.

An example X-ray diffraction pattern from the tensile experiment is shown in Fig. 9a, together with a line profile at the 0° azimuth angle (Fig. 9b). The measured changes in $d_{00.2}$, referred to here as the 'crystal strains' for convenience, are compared with the bulk strain data in Fig. 10. The crystal strains are identified for the two positions (H1 and H2) and the specimen two rotation angles (0° and 90°) that sample four different gauge volumes of microstructure. The reported errors include the combined effects of the measurement and correction uncertainties described earlier.

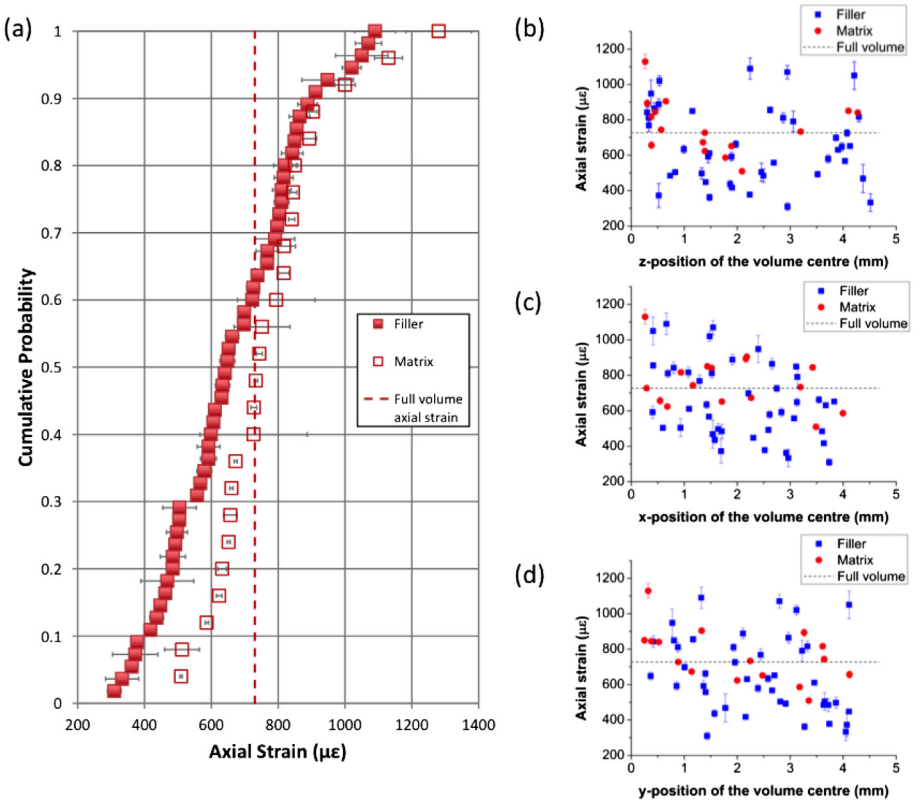

Fig. 8. The variation of axial strain at an applied tensile load of 250 N (stress ~ 7.5 MPa), measured by image correlation, in regions of matrix and filler particles; a) distributions of strain compared with the average bulk strain; and variation of strain with b) vertical *z*, c) horizontal *x* and d) horizontal *y* position in the cropped tomographed volume. (A colour version of this figure can be viewed online.)

The axial and transverse changes in the crystal strains were obtained at the 90° and 0° azimuth angles.

The axial crystal strains in the tensile specimen increase with increasing bulk strain (Fig. 10a); the data are presented for the change in $d_{00.2}$ at the 90° azimuth angle, concurrent with the measured bulk tensile strain. The transverse crystal strains (at the 0° azimuth) appear to become less compressive as the measured transverse bulk strains due to Poisson contraction increase in magnitude (Fig. 10b). The crystal strain data are shown in Fig. 10c as a function of the peak tensile bulk strain, i.e. the loaded data are measured at the peak strain, and unloaded data are shown as function of the peak strain applied before unloading. This reveals that on the first load cycle the axial crystal strain does not increase significantly, but on unloading there is a significant decrease of the axial $d_{00.2}$ by approximately 3×10^{-4} Å, which is equivalent to a strain of 85 με. In the subsequent cycles, the axial crystal strain under load increases with the applied tensile bulk strain whereas the unloaded crystal strain returns to close to the initial value, and does not measurably change further. The transverse crystal strains also show different behaviour in the first load cycle; they decrease when first loaded, while the axial crystal strains do not increase. The transverse crystal strains then do not change measurably when the load is removed and remain effectively constant in the subsequent cycles with increasing axial crystal strain (Fig. 10d). The outlier data with high tensile transverse bulk strain for the H2 position at the 0° rotation in the final load cycle (Fig. 10b) were recorded just before the specimen had failed.

3.3. Neutron diffraction: bending loading

An example neutron time-of-flight diffraction spectrum for Bank 1 (in-plane or longitudinal strain) for the bending loading

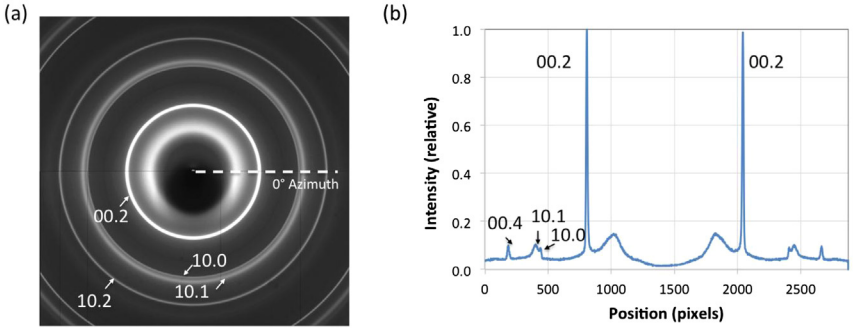

Fig. 9. Example of X-ray diffraction data; a) image of the diffration rings, b) a line profile of the intensity across the diffraction rings (at 0° azimuth angle). The diffraction peaks at 00.2, 10.0, 00.4 and 10.1 are indicated. (A colour version of this figure can be viewed online.)

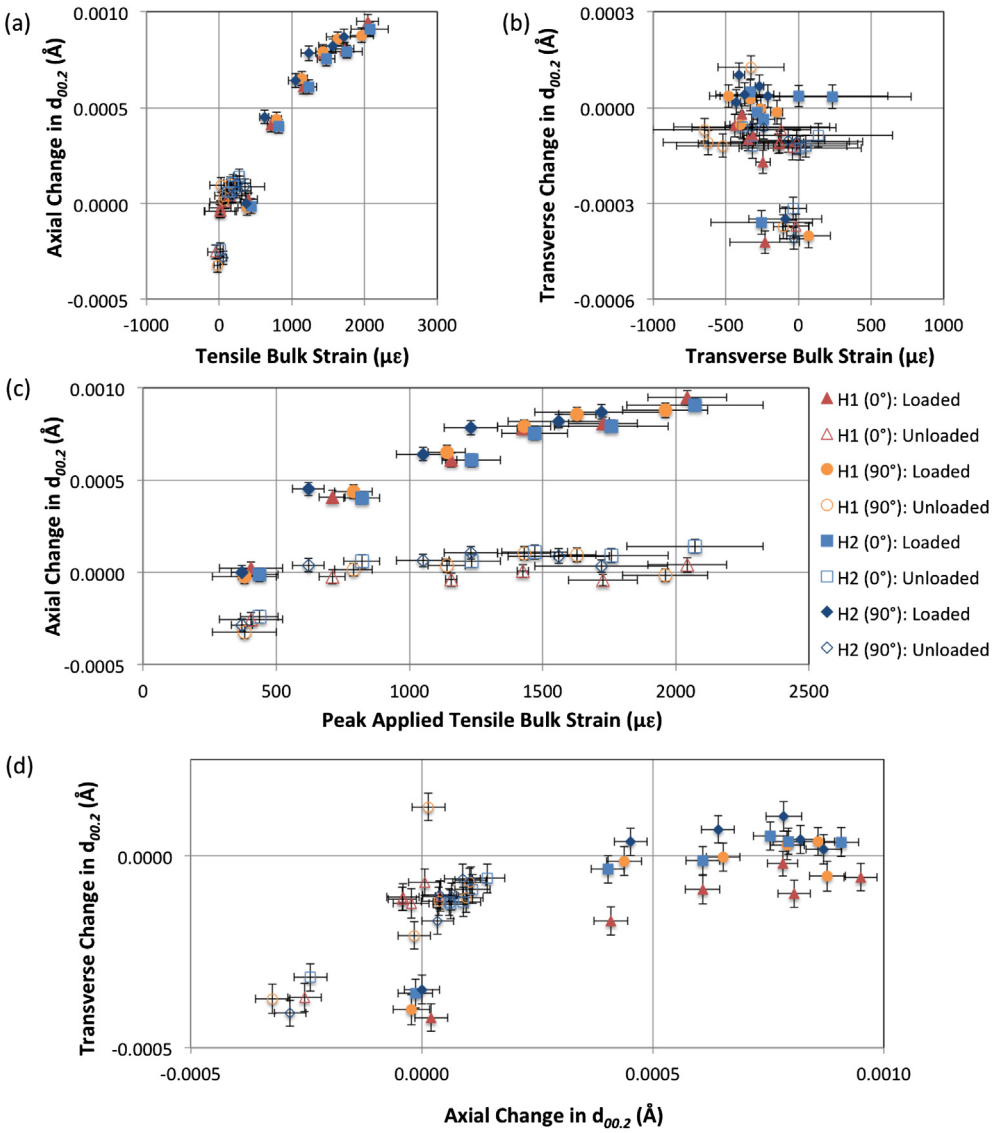

Fig. 10. The change in $d_{(00.2)}$: a) with the applied tensile bulk strain, b) at the transverse bulk strain both measured concurrently, c) as a function of the peak tensile bulk strain applied at or before the measurement; d) a comparison of the concurrent axial and transverse measurements. (Data shown for the loaded and unloaded state at locations H1 & H2, in the 0° and 90° orientations – see common legend). (A colour version of this figure can be viewed online.)

experiment is shown in Fig. 11. As with the X-ray data, only the changes for the lowest stiffness basal plane are considered here. Measurements at each of the six positions in the initial free standing condition provided the reference, against which the change in $d_{00.2}$ was measured. The obtained data for change in $d_{00.2}$ as a function of bulk longitudinal strain at the IGV position are presented in Fig. 12, and are also compared with the data from the tensile specimen, obtained by synchrotron X-ray diffraction. Within the scatter, the data from different measurement positions provide self-consistent measurement of the relation between crystal and bulk in-plane strain. There is good agreement between the neutron and X-ray measurement. Indeed, both show a tendency for non-linear behaviour with tensile strains, while the neutron data in the compressive region are essentially linear. A least-squares linear fit to the neutron data with compressive applied strains is shown in Fig. 12.

The initial tests of fully strain gauged flexure specimens, off the beamline, provided data for the relation between applied load and the surface strain gauges. The example data in Fig. 13 show a linear increase of the surface strains with applied bending stress, which

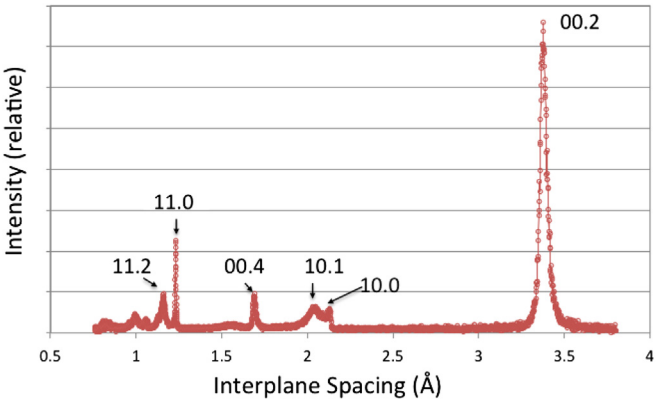

Fig. 11. Example of neutron diffraction spectrum obtained from the flexure specimen. The diffraction peaks at 00.2, 00.4, 10.0, 11.2, 11.0 and 10.1 are indicated. (A colour version of this figure can be viewed online.)

was calculated from the applied load and simple slender beam theory [90]. A residual strain remains after unloading in each cycle, and this increases with the peak applied bending surface strain. That experiment also provided typical data for the unloading elastic modulus, and these are reported from the surface strain gauges in Table 2. In this example, the specimen failed in the fourth cycle at the peak bending stress – prior to this, the elastic modulus in bending was approximately constant.

The magnitudes of the residual strains after unloading, for both the flexure and tensile diffraction experiments, are presented in Fig. 14. For the flexure specimen, there is a clear trend of increasing residual bulk in-plane strain with increasing magnitude of applied strain (tensile and compressive). These data are from the strain gauges on the tensile and compressive surfaces (Fig. 14a). Corresponding behaviour is also observed in the tensile specimen; bulk tensile pre-strain leads to a small permanent tensile bulk strain (Fig. 14b). The diffraction data show different trends: for the bending specimen, the residual crystal strains tend to compression with increasing tensile peak bulk strain, and vice versa (Fig. 14a). Conversely, for the tensile specimen, other than the decrease after the first cycle, there is no significant residual crystal strain measured (Fig. 10c).

4. Discussion

The bulk elastic moduli and the Poisson's ratio obtained by image correlation analysis of radiographs are in good agreement with the expected values for this graphite [75], which gives high confidence in the accuracy of displacement measurements by this technique. The tensile experiment also demonstrates the expected degradation of elastic modulus with increasing applied tensile strain due to damage [35,36] (Table 1). The generally lower modulus obtained for the longer measurement gauge length can be attributed to microstructure heterogeneity. In contrast, the elastic modulus in bending is not measurably affected by loading (Table 2). The difference in the response between tensile and flexure specimens is due to the strain gradient in the latter specimen, in which the larger volume that experiences non-damaging low strains dominates the overall stiffness.

The maximum strain of the bending specimen, which is approximately 40% larger than the maximum average strain sustained in the tensile test is in the expected range of 40–70% [23], although the tensile strain is 20% lower than expected for this grade [75]. The image correlation analysis undertaken on the tensile test specimen tomographs reveals there is a degree of specimen flexure, despite the use of a self-aligning jig (Fig. 7b). The ASTM standard C565 [78] for graphite tensile strength measurement does not specify a quantitative limit for flexure. But ASTM C749 for measurement of the tensile stress/strain of graphite [91], permits bending stresses at the surface (described as 'parasitic' stresses that are due to misalignment) of up to 5% of the mean stress; the average strain gradient (Fig. 7b) is equivalent to a 17% parasitic surface strain, which would account for the lower than average tensile strength.

Both the tensile and flexure experiments demonstrate the expected development of 'permanent set' encountered when testing non-irradiated graphite [20] (Figs. 5 and 14). The image correlation analysis of radiographs shows this occurs at the microstructure length-scale (Fig. 3), and the image correlation of tomographs of selected volumes confirms this strain localization is due to the heterogeneous microstructure (Fig. 7a). It is noteworthy that this localized strain, observed in the tensile specimen, is not recovered fully when the load is removed, demonstrating that some microstructure regions deform in-elastically. This is attributed to a small misalignment of the tensile specimen, which causes the gradient of total strain across the specimen observed in Fig. 7b, together with a similar gradient of the inelastic bulk axial strain under load. On unloading, this introduces a residual compressive axial bulk strain, and an associated residual tensile transverse bulk strain (as observed in Fig. 5b and c), similar to the residual strains that arise when the bend specimens tested in flexure.

The diffraction analyses, which measure the elastic strain in the graphite crystals as the change in $d_{00.2}$, provide several interesting observations. There is very good agreement between the neutron and X-ray measurements, since both show non-linear behaviour of the crystal strains as a function of the applied tensile strain. The neutron data show the deformation is more linear in the compressive region (Fig. 12), obtained in the bend specimen geometry. Such non-linearity in the response of this and related graphites has been proposed to be due to an inelastic mechanism such as microcracking or plastic deformation by basal slip [33]. Both would reduce the increase inelastic strain with increasing applied

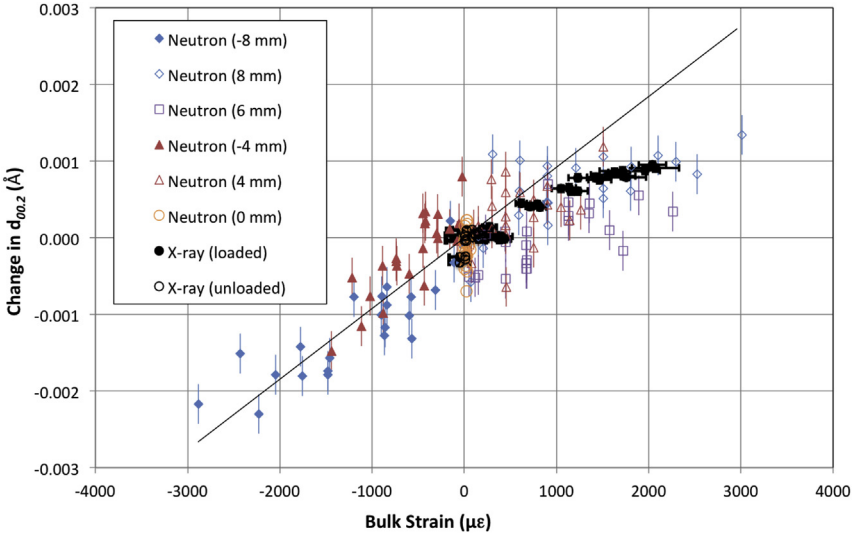

Fig. 12. The change in $d_{00.2}$ with the bulk strain at the measurement position for both neutron diffraction (flexure specimen) and X-ray diffraction (tensile specimen). A linear least-squares fit to the neutron data for compressive bulk strain is shown (gradient 9×10^{-7} A/με). The error bars for the change in $d_{00.2}$ are the measurement uncertainty equivalent to a strain error of 50 με (see Appendix). (A colour version of this figure can be viewed online.)

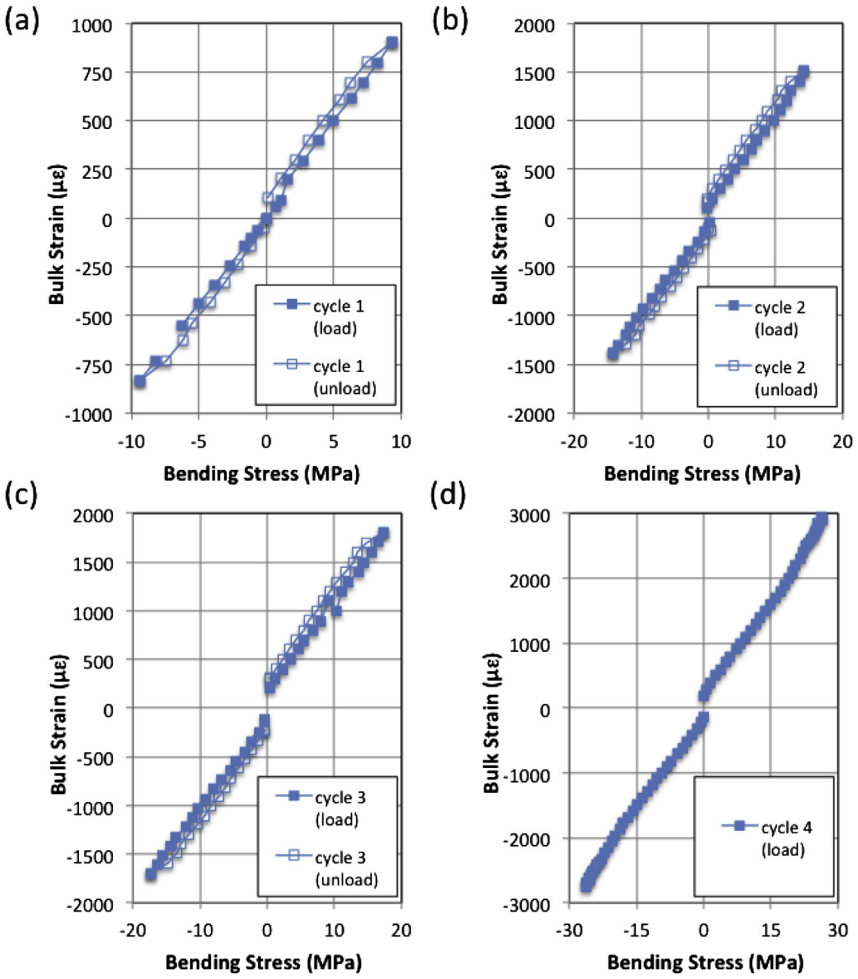

Fig. 13. Example data for the variation of bulk in-plane surface strain with bending stress for a flexure loaded specimen (identical sample to that examined by neutron diffraction). The sample failed in cycle 4 under load. (A colour version of this figure can be viewed online.)

Table 2
The effect of applied peak stress on elastic modulus, measured in bending loading and unloading (from Fig. 13).

Cycle	Peak bending stress (MPa)	Peak strain (με) (Tensile surface)	Peak strain (με) (Compressive surface)	Elastic modulus (GPa) (Loading, tensile surface)	Elastic modulus (GPa) (Unloading, tensile surface)
1	9.36	904 ± 5	−833 ± 5	10.38 ± 0.19	11.12 ± 0.34
2	14.17	1506 ± 5	−1389 ± 5	10.59 ± 0.15	10.53 ± 0.21
3	17.40	1800 ± 5	−1697 ± 5	10.87 ± 0.21	10.59 ± 0.22
4	26.40	2950 ± 5	−2741 ± 5	9.89 ± 0.12	–

strain, though the clear effect on tensile behaviour observed here suggests that microcracking dominates in tension, as expected [36].

It is significant that in first load cycle of the tensile experiment the axial elastic strain, measured as the change in $d_{00.2}$ in the tensile direction, does not increase with the applied strain, and it decreases after unloading. Although the elastic strain that is measured under load subsequently increases with applied tensile strain, the residual elastic strain upon unloading is zero; i.e. $d_{00.2}$ returns to a value close to that of the as-received material. Similarly, the transverse elastic strain, which is measured as the change in $d_{00.2}$ at the 0° azimuth angle, is compressive for the first load cycle, does not change measurably when the load is removed, and then returns to zero on the next loading, at which it remains thereafter. In the bending specimen, the residual elastic strains tend to become compressive with increasing tensile permanent set, and vice versa (Fig. 14). This behaviour is a simple consequence of the elastic spring-back with a gradient of permanent deformation – tensile plastic strain leads to compressive elastic spring-back. Unfortunately, the neutron data are not sufficiently sensitive to record the elastic strain decrease on first loading that is observed by X-ray diffraction in the tensile experiment.

The elastic strain behaviour in the tensile experiment requires further explanation. As graphitization takes place at temperatures in excess of 2500 °C, and due to the graphite crystal structure being highly anisotopic due to the weak interplanar forces of the basal planes, significant thermal residual stresses develop within the graphite microstructure as it cools to ambient temperature. This is the origin of Mrozowski cracks on (00.1) planes [28]. The microstructure may be regarded to be in a state of equilibrium between these stresses and the critical stresses for micro-cracking and basal slip, which act to relax the thermal stresses that are due to the thermal strains. Experimental measurements show that tensile residual stress exists in the Gilsocarbon filler particles of this graphite grade, with compression in the matrix [29]. An increase in

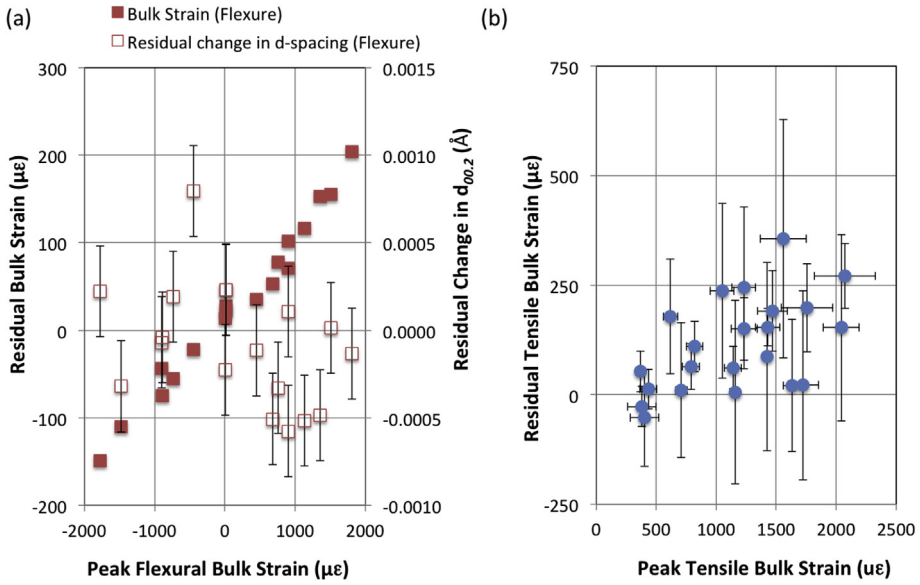

Fig. 14. The development of residual strains after unloading from the peak strain; a) tensile specimen; b) flexure specimen. The residual change in $d_{00.2}$ after unloading from the peak strain at that position is also shown for the neutron data. (A colour version of this figure can be viewed online.)

applied strain would lead to further micro-cracking, and the permanent set in the tensile experiment data confirms that inelastic deformation occurs as the applied strain increases. The image correlation of radiographs demonstrates that this is localized at the millimeter length scale of the microstructure, and that some of this strain is not recoverable. This appears to provide a reasonable cause for the negligible change in the axial $d_{00.2}$ when the tensile load is first applied, where the static value represents the lattice strain of the elastic stress that is in equilibrium with the critical stresses for microcracking and slip. On removal of the applied load, the axial crystal elastic stress is relaxed, and $d_{00.2}$ decreases in this direction. Compressive transverse crystal strain in the first loading is consistent with the compressive transverse bulk strain from the Poisson contraction. This simple explanation implies, however, that axial $d_{00.2}$ should not continue to increase as the applied tensile strain increases, which is contrary to the observations. It does not explain why $d_{00.2}$ returns to the original value when unloaded in the subsequent cycles. Moreover, the transverse crystal strains under load would be expected to become increasingly compressive, and this is not observed. Microcracking, as a mechanism to relieve tensile strain in brittle heterogeneous materials [92] has been proposed to saturate with increasing tensile strain [93]. This may explain the stability of the unloaded $d_{00.2}$, and the gradual increase in $d_{00.2}$ with applied load is observed in Fig. 10c. However, the mechanisms may relate closely with the complex connected network of crystals that are arranged in the constituents of the graphite microstructure at a length-scale equal to or below the meso-scale. The diffraction analysis, which has a large gauge volume, samples microstructure that contains both filler particles and matrix to provide an average effect of the localized strains. A higher resolution analysis, utilizing micro-Raman spectroscopy for surface observations or micro-scale testing of graphite samples of isolated matrix regions and filler particles using synchrotron diffraction, might provide the necessary understanding.

5. Conclusion

- Neutron and X-ray diffraction experiments provide insights to the response to loading of the IM1-24 polygranular Gilsocarbon microstructure. Synchrotron X-Rays have very high signal to noise ratio, compared with neutrons, and this provides greater measurement precision.
- When measured over a sufficient gauge length of several mm image correlation with radiographs and tomographs can measure bulk elastic properties with a precision similar to strain gauges. Over a shorter gauge length, more qualitative data are obtained due to the heterogeneity of inelastic and elastic deformation.
- Both neutron and X-ray studies show the application of tensile strain reduces the bulk elastic modulus.
- In compression, a linear relation is observed between the elastic strains in the graphite crystals and the applied strain. In tension, this relationship is non-linear.
- The microstructure of the studied graphite contains significant residual elastic strains, which appear to be relaxed by the application of tensile strain. It is deduced this is accompanied by microcracking.

Acknowledgements

The authors are very thankful to M. Mostafavi (University of Sheffield), M. Jordan (University of Oxford) and also K. Hallam and A. Andriot (University of Bristol) for their assistance during these experiments and helpful discussions. The awards of experimental time on I12 at the Diamond Light Source (EE9036 – Strain-mapping in quasi-brittle materials by diffraction) and ENGIN-X at ISIS (RB1320187 – A Novel In-situ Approach to Evaluate the Process Zone in Quasi-brittle Materials under Bending) are acknowledged. The research was supported by the UK Engineering and Physical Science Research Council (EPSRC) under awards EP/J01992/1, EP/J019801/1 and EP/H025286 (QUBE: QUasi-Brittle fracture: a 3D Experimentally-validated approach). Dr Brian Connolly (University of Birmingham) is thanked for the loan of the tensile loading rig, funded by EPSRC (EP/H025286/1 – Long Term, In Situ Material Degradation Studies Utilizing High Resolution Laboratory X-ray Tomography). The support of TJM by the Oxford Martin School (Nuclear Programme) and of YeV by EDF Energy, who provided the material, is gratefully acknowledged. PEJF acknowledges Wolfson College, Oxford, for facilitating the collaboration.

Appendix. Cross-correlation analysis of diffraction peak shifts

A cross-correlation method has been implemented in this work to improve the speed and precision of the measurement of sub-pixel shifts of a diffraction peak. Cross-correlation has been proposed previously for the analysis of strains by X-ray diffraction due to its insensitivity to peak shape and ability to work with less information [94], but it is not routinely used. In general cross-correlation is used in the analysis of small shifts with high precision in high-resolution EBSD (electron backscatter diffraction) analysis [95]. The approach implemented here is based on analysis of the cross-correlation product between the reference diffraction peak, which is obtained with the specimen in the initial unloaded state and the loaded peak.

These data are subsequently referred to as the 'original signal' and 'delayed signal'; the difference between these can be regarded as a 'time delay'. The expression for the cross-correlation between the two signals is given in Equation (A1); f and g respectively are the original and delayed signal. For $g(t) = f(t - \delta)$, the convolution product is maximised at $\tau = \delta$.

$$(f*g)(\tau) \underline{\underline{\text{def}}} \int_{-\infty}^{\infty} f(t)g(t+\tau)\,dt \tag{A1}$$

Due to the nature of the signal sampling, f and g are discrete functions; so determining the argument of the maximum of the cross-correlation product will only provide the integer part of the delay value. However, an iterative least-square peak fitting method, applied to the cross-correlation function between the original and delayed signal, allows determination of the delay with higher precision. We have found that performing the latter step with the Fourier transform of the correlation function achieves greater speed (approximately a factor of 150 times, compared to cross-correlation in the time domain) and robustness to signal noise (compared to conventional analysis methods). The shape of the cross-correlation peak is a function of signal shape, so the nature of the peak used during the fitting should be adapted to those signals (i.e. pseudo-Voigt in the case of diffraction).

In the implementation of this 'XCORR' method, a first pass analysis in the time domain allows retrieval of the integer part of the delay by finding the cross-correlation function maximum. This integer delay is then corrected using the delayed signal within Fourier space by applying a phase shift (Equation (A2)); this step could be considered to be a 'time-domain registration' of the signals, similar to the pre-analysis step of displacement registration that is used in image correlation techniques.

$$x[n] \leftrightarrow X[k]$$

$$x[n-D] \leftrightarrow e^{\frac{-2\pi jkD}{N}} X[k] \tag{A2}$$

The sub-sampling time delay appears as the gradient of the phase of the convolution product in the Fourier domain. It can be extracted by a simple linear fit, weighted by the signal amplitudes for noise reduction purposes [96].

The analysis method is insensitive to the magnitude of the time delay, but is dependent of the peak shape, which differs for neutron and X-ray diffraction data (Fig. A1). The full width of the $d_{00.2}$ peak is of the order of 0.15 Å, and the neutron data are at discrete intervals of 4×10^{-4} Å, whereas the intervals of the X-ray data are 5.3×10^{-3} Å around the position of the $d_{00.2}$ peak. The pixel size actually varies across the full diffraction spectra due to the intersection of the diffraction cone with the image plane, but the effect is negligible around individual peaks. The neutron TOF bins are regarded as equivalent to pixels; both are data at discrete intervals. The signal to noise ratios (SNR) for the neutron and X-ray peaks are 23.3 dB and 46.7 dB respectively, measured by determining the noise power as the variance on the profile baseline and the signal power as the mean square of the data [97]. In the analysis of the diffraction data using Bragg's Law, it is necessary to know the inter-planar separation, $d_{(hkl)}$, of the reference peak in order to calculate its change using the measured change in diffraction angle, $\Delta 2\theta$, which is provided by the cross-correlation 'time delay'. This was obtained by application of the conventional least-square peak fitting method to find the peak position, from which $d_{00.2}$ was calculated using the Ceria calibration. For the X-ray data, the ring diameter was measured to obtain 4θ.

To assess the sensitivity of the above cross-correlation analysis with respect to the conventional analysis, e.g. as described in Ref. [98], a benchmark shift of 0.5 pixels was applied to synthetic pseudo-Voigt peaks that were of similar width to either the X-ray or neutron data in terms of the number of discrete data points across the peak. Additive white Gaussian noise was applied to both the peaks, and the peak shift was then measured; the error from the known shift provides the measurement uncertainty. The effect of varying the SNR is presented in Fig. A2, which also shows the influence of signal pre-conditioning methods that are commonly used in data treatment, e.g. Ref. [99] (only the X-ray examples are presented for clarity); median (order 10) and wavelet filters (Symlet 8 with Stein's unbiased risk estimate thresholding) were applied. The changes in the peak shape by filtering are detrimental to measurements made with the conventional method, especially in the case of wavelet filtering that induces artifacts in the peak shape. The outcome demonstrates that the cross-correlation method is more robust. For the X-ray peaks, cross-correlation achieved better precision than the conventional method for signal to noise ratios above 30 dB, with comparable results below this. The two methods are closely equivalent for the neutron peaks since these are relatively broad compared to the X-ray data, which causes the slightly greater error.

This analysis provides an estimate of the measurement uncertainty in the experimental data for the change in $d_{00.2}$, via the error in the determination of the benchmark peak shift for an equivalent SNR. At 25 dB, which is representative of the neutron data, the error in the $d_{00.2}$ shift is 7.86×10^{-5} Å and 7.9×10^{-5} Å respectively for the conventional and the XCORR method with a neutron peak. The strain measurement error is approximately 25 με. This is within the expected precision of 50 με for neutron diffraction [85]. The latter includes additional errors due to positioning that are not accommodated in this assessment of the intrinsic measurement uncertainty.

At 45 dB, which is representative of the X-ray data, the uncertainty in the $d_{00.2}$ shift for an X-ray peak is 3.9×10^{-5} Å for cross-correlation and 5.3×10^{-5} Å for the conventional method. The expected strain uncertainties are thus 12 με and 18 με respectively. This is quite consistent with the variability that is observed with Azimuth angle around the full $d_{00.2}$ diffraction ring (Fig. A3). In this example the variances, relative to smooth fits through the data, are 3.5×10^{-5} Å and 3.9×10^{-5} Å for the cross-correlation and conventional analyses respectively. The agreement between the expected and measured errors is attributed to the fine correction for specimen positioning by the use of digital image correlation of radiographs, as described in the main text; this correction could not be applied to the neutron observations.

Interestingly, cross-correlation tends to report lower shifts than the conventional analysis as the smaller values are approached at the 0° and 180° azimuth angles. Comparisons of the $d_{00.2}$ peak shifts obtained by the conventional method and the cross-

correlation methods, for all of the data obtained in the graphite tensile and bending experiments, are presented in Fig. A4; the equivalence of the analysis methods for neutron and X-ray diffraction is clear. As in Fig. A3, the shifts measured by cross-correlation tend to be lower than the conventional method at smaller values. The reason for this small bias, which is of the order of the measurement uncertainty, is not certain, but it may be an artifact of the assumed peak shape. The cross-correlation analysis method has been used in this work due to its greater speed, robustness and improved precision, at least for the X-ray data.

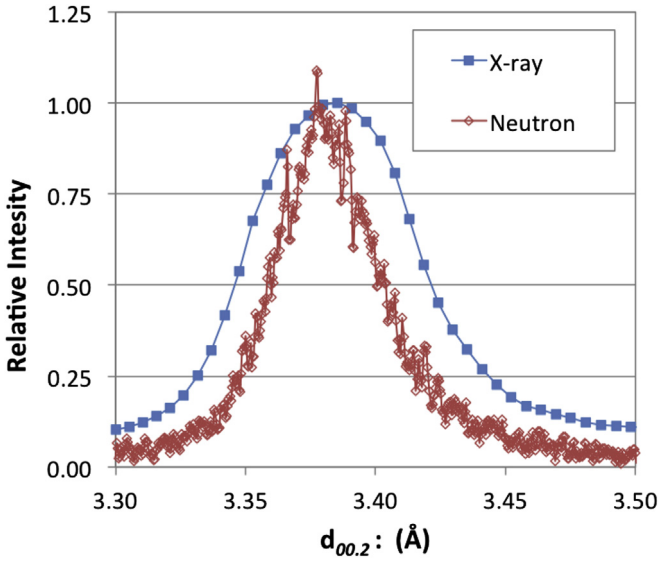

Fig. A1. Examples of the $d_{00.2}$ diffraction peak measured by neutron diffraction (data at intervals of 4×10^{-4} Å) and synchrotron X-ray diffraction (data at intervals of ~5.3×10^{-3} Å at the peak).

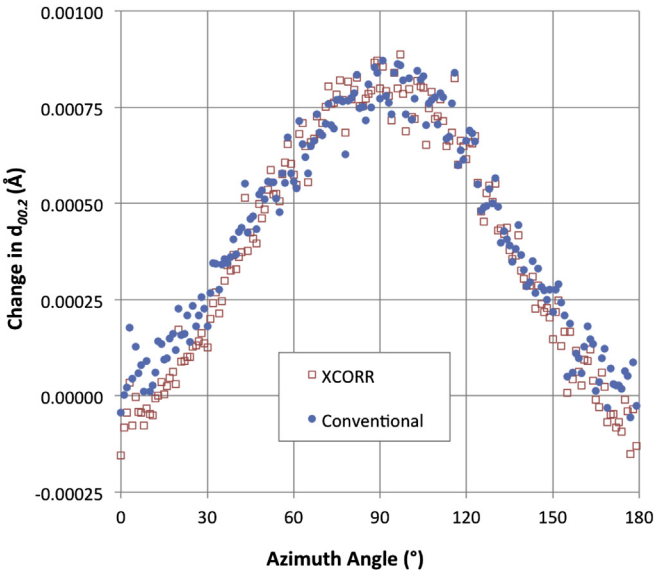

Fig. A3. An example of the calculated change in $d_{00.2}$ as a function of azimuth angle about the X-ray 00.2 diffraction ring, analysed by cross-correlation (XCORR) and the conventional method; in both cases, a 1° bin size was used. These data are for position H1, in the 0° orientation, and were obtained by comparison of diffraction image at a stress of 12.3 MPa, compared to the original unloaded state. Sample movements have been corrected for.

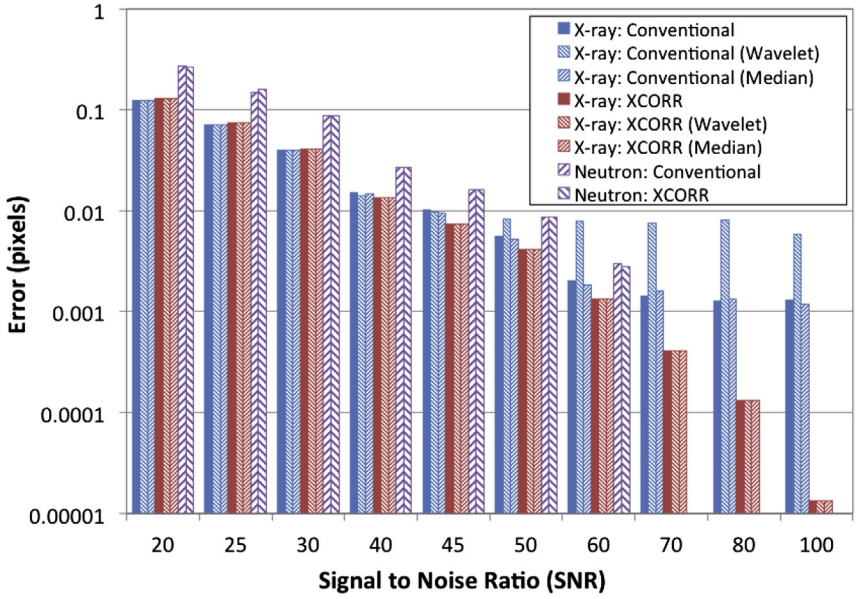

Fig. A2. The error (uncertainty) in the calculated peak shift (a benchmark shift of 0.5 pixel), as a function of signal to noise ratio, for the conventional and cross-correlation (XCORR) analysis methods applied peaks representative of X-ray and neutron $d_{00.2}$ diffraction. The effect of filters, applied to the X-ray peaks, is also presented.

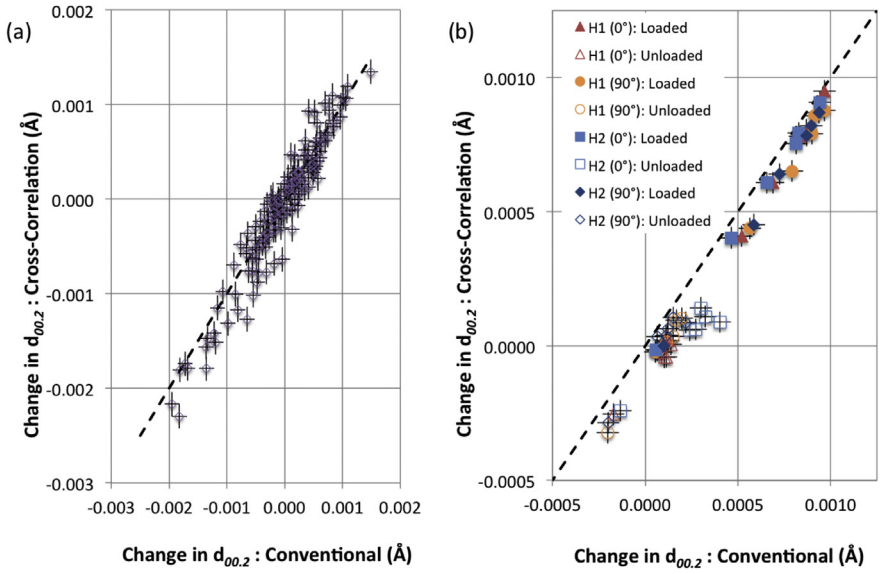

Fig. A4. Comparison of the shift in $d_{00.2}$ measured by the conventional and cross-correlation methods for a) neutron diffraction, and b) synchrotron X-ray diffraction. The error bars are the expected uncertainty in the analysis, obtained for the signal to noise ratio of the $d_{00.2}$ peak (Fig. A2).

References

[1] F.J. Luque, J.D. Pasteris, B. Wopenka, M. Rodas, T.F. Barrenechea, Natural fluid-deposited graphite: mineralogical characteristics and mechanisms of formation, Am. J. Sci. 298 (1998) 471–498.

[2] J.P. Redmond, P.L. Walker, Gas content of graphites, Nature 186 (1960) 72–74, http://dx.doi.org/10.1038/186072a0.

[3] M. Dee, C. Bronk Ramsey, Refinement of graphite target production at ORAU, Nucl. Instrum. Methods Phys. Res. Sect. B Beam Interact. Mater. Atoms 172 (2000) 449–453.

[4] D.D.L. Chung, Electrical applications of carbon materials, J. Mater. Sci. 39 (2004) 2645–2661, http://dx.doi.org/10.1023/B: JMSC.0000021439.18202.ea.

[5] Z. Yang, J. Zhang, M.C.W. Kintner-Meyer, X. Lu, D. Choi, J.P. Lemmon, et al., Electrochemical energy storage for green grid, Chem. Rev. 111 (2011) 3577–3613, http://dx.doi.org/10.1021/cr100290v.

[6] J. Schmidt, K.D. Moergenthaler, K.-P. Brehler, J. Arndt, High-strength graphites for carbon piston applications, Carbon 36 (1998) 1079–1084, http://dx.doi.org/10.1016/S0008-6223(98)00081-5.

[7] J.P. Bonal, A. Kohyama, J. Van Der Laan, L.L. Snead, Graphite, ceramics, and ceramic composites for high-temperature nuclear power systems, MRS Bull. 34 (2009) 28–34.

[8] B.T. Kelly, Graphite – the most fascinating nuclear material, Carbon 20 (1982) 3–11, http://dx.doi.org/10.1016/0008-6223(82)90066-5.

[9] R. Moskovic, P.E.J. Flewitt, E. Schlangen, G. Smith, A.G. Crocker, A. Hodgkins, et al., Understanding fracture behaviour of PGA reactor core graphite: perspective, Mater. Sci. Technol. 30 (2014) 129–145, http://dx.doi.org/10.1179/1743284713Y.0000000354.

[10] B.J. Marsden, G.N. Hall, Comprehensive Nuclear Materials, vol. 4, Elsevier, 2012, http://dx.doi.org/10.1016/B978-0-08-056033-5.00092-6.

[11] T. Abram, S. Ion, Generation-IV nuclear power: a review of the state of the science, Energy Policy 36 (2008) 4323–4330, http://dx.doi.org/10.1016/j.enpol.2008.09.059.

[12] S. Saito, T. Tanaka, Y. Sudo, Present status of the high temperature engineering test reactor (HTTR), Nucl. Eng. Des. 132 (1991) 85–93.

[13] K.Y. Wen, T.J. Marrow, B.J. Marsden, The microstructure of nuclear graphite binders, Carbon 46 (2008) 62–71, http://dx.doi.org/10.1016/j.carbon.2007.10.025.

[14] T.D. Burchell, A microstructurally based fracture model for polygranular graphites, Carbon 34 (1996) 297–316, http://dx.doi.org/10.1016/0008-6223(95)00171-9.

[15] N. Nemeth, A. Walker, E. Baker, P. Murthy, R. Bratton, Large-scale Weibull analysis of H-451 nuclear-grade graphite rupture strength, Carbon 58 (2013) 208–225, http://dx.doi.org/10.1016/j.carbon.2013.02.054.

[16] S.-H. Chi, Specimen size effects on the compressive strength and Weibull modulus of nuclear graphite of different coke particle size: IG-110 and NBG-18, J. Nucl. Mater. 436 (2013) 185–190, http://dx.doi.org/10.1016/j.jnucmat.2012.09.023.

[17] C. Karthik, J. Kane, D.P. Butt, W.E. Windes, R. Ubic, Microstructural characterization of next generation nuclear graphites, Microsc. Microanal. 18 (2012) 272–278, http://dx.doi.org/10.1017/S1431927611012360.

[18] S. Chi, G. Kim, Mrozowski cracks and oxidation behavior of IG-110 and IG-430 nuclear graphites, in: Transactions of the Korean Nuclear Society Spring Meeting, Chuncheon, Korean Nuclear Society (Republic of Korea), Korea, 2006.

[19] Y.-S. Lim, S.-H. Chi, K.-Y. Cho, Change of properties after oxidation of IG-11 graphite by air and CO2 gas, J. Nucl. Mater. 374 (2008) 123–128, http://dx.doi.org/10.1016/j.jnucmat.2007.07.015.

[20] R. Taylor, R.G. Brown, K. Gilchrist, E. Hall, A.T. Hodds, B.T. Kelly, et al., The mechanical properties of reactor graphite, Carbon 5 (1967) 519–531, http://dx.doi.org/10.1016/0008-6223(67)90029-2.

[21] M. Mostafavi, S.A. McDonald, H. Çetinel, P.M. Mummery, T.J. Marrow, Flexural strength and defect behaviour of polygranular graphite under different states of stress, Carbon 59 (2013) 325–336, http://dx.doi.org/10.1016/j.carbon.2013.03.025.

[22] P.-Y. Tang, Interpretation of bend strength increase of graphite by the couple-stress theory, Comput. Struct. 16 (1983) 45–49, http://dx.doi.org/10.1016/0045-7949(83)90146-3.

[23] J. Brocklehurst, M. Darby, Concerning the fracture of graphite under different test conditions, Mater. Sci. Eng. 16 (1974) 91–106, http://dx.doi.org/10.1016/0025-5416(74)90143-8.

[24] M.P. Hindley, D.C. Blaine, A.A. Groenwold, T.H. Becker, Failure prediction of full-size reactor components from tensile specimen data on NBG-18 nuclear graphite, Nucl. Eng. Des. 284 (2015) 1–9, http://dx.doi.org/10.1016/j.nucengdes.2014.12.011.

[25] S. Yu, X. Fang, H. Wang, C. Li, Failure probability study of HTR graphite component using microstructure-based model, Nucl. Eng. Des. 253 (2012) 192–199, http://dx.doi.org/10.1016/j.nucengdes.2012.08.019.

[26] E.J. Seldin, Stress-strain properties of polycrystalline graphites in tension and compression at room temperature, Carbon 4 (1966) 177–191, http://dx.doi.org/10.1016/0008-6223(66)90079-0.

[27] L. Delannay, P. Yan, J.F.B. Payne, N. Tzelepi, Predictions of inter-granular cracking and dimensional changes of irradiated polycrystalline graphite under plane strain, Comput. Mater. Sci. 87 (2014) 129–137, http://dx.doi.org/10.1016/j.commatsci.2014.02.008.

[28] S. Mrozowski, Mechanical Strength, Thermal Expansion and Structure of Cokes and Carbons. Proc. 1st and 2nd Conferences on Carbon, Waverly Press, Buffalo, NY, 1956, p. 31.

[29] R. Krishna, A.N. Jones, R. Edge, B.J. Marsden, Residual stress measurements in polycrystalline graphite with micro-Raman spectroscopy, Radiat. Phys. Chem. 111 (2015) 14–23, http://dx.doi.org/10.1016/j.radphyschem.2015.02.007.

[30] M.C. Smith, Effects of prestrain on the tensile properties of graphite, Carbon 2 (1964) 269–274, http://dx.doi.org/10.1016/0008-6223(64)90041-7.

[31] L.M. Gillin, Deformation characteristics of nuclear grade graphites, J. Nucl. Mater. 23 (1967) 280–288, http://dx.doi.org/10.1016/0022-3115(67)90160-2.

[32] S. Sato, H. Awaji, H. Akuzawa, Fracture toughness of reactor graphite at high temperature, Carbon 16 (1978) 95–102, http://dx.doi.org/10.1016/0008-6223(78)90004-0.

[33] G.B. Neighbour, B. McEnaney, Creep and recovery in graphites at ambient temperature: an acoustic emission study, Carbon 32 (1994) 553–558, http://dx.doi.org/10.1016/0008-6223(94)90071-X.

[34] G.B. Neighbour, B. McEnaney, M. Phillips, Acoustic emission responses from cyclic loading of a nuclear graphite, Carbon 30 (1992) 359–363, http://dx.doi.org/10.1016/0008-6223(92)90031-Q.

[35] G.M. Jenkins, Fracture in reactor graphite, J. Nucl. Mater. 5 (1962) 280–286, http://dx.doi.org/10.1016/0022-3115(62)90068-5.

[36] S. Yoda, M. Eto, T. Oku, Change in dynamic young's modulus of nuclear-grade isotropic graphite during tensile and compressive stressing, J. Nucl. Mater. 119 (1983) 278–283, http://dx.doi.org/10.1016/0022-3115(83)90204-0.

[37] M.R. Ayatollahi, A.R. Torabi, Failure assessment of notched polycrystalline graphite under tensile-shear loading, Mater. Sci. Eng. A 528 (2011) 5685–5695, http://dx.doi.org/10.1016/j.msea.2011.04.066.

[38] F. Berto, P. Lazzarin, Recent developments in brittle and quasi-brittle failure assessment of engineering materials by means of local approaches, Mater. Sci. Eng. R Rep. 75 (2014) 1–48, http://dx.doi.org/10.1016/j.mser.2013.11.001.

[39] Z. Zou, S.L. Fok, S.O. Oyadiji, B.J. Marsden, Failure predictions for nuclear graphite using a continuum damage mechanics model, J. Nucl. Mater. 324 (2004) 116–124, http://dx.doi.org/10.1016/j.jnucmat.2003.09.005.

[40] T.H. Becker, M. Mostafavi, R.B. Tait, T.J. Marrow, An approach to calculate the J-integral by digital image correlation displacement field measurement, Fatigue Fract. Eng. Mater. Struct. (2012) 971–984, http://dx.doi.org/10.1111/j.1460-2695.2012.01685.x.

[41] H. Li, J. Li, G. Singh, A. Fok, Fracture behavior of nuclear graphite NBG-18, Carbon 60 (2013) 46–56, http://dx.doi.org/10.1016/j.carbon.2013.03.055.

[42] R. Moskovic, P.J. Heard, P.E.J. Flewitt, M.R. Wootton, Overview of strength, crack propagation and fracture of nuclear reactor moderator graphite, Nucl. Eng. Des. 263 (2013) 431–442, http://dx.doi.org/10.1016/j.nucengdes.2013.05.011.

[43] P. Ouagne, G.B. Neighbour, B. McEnaney, Crack growth resistance in nuclear graphites, J. Phys. D Appl. Phys. 35 (2002) 927–934, http://dx.doi.org/10.1088/0022-3727/35/9/315.

[44] A. Hodgkins, T.J. Marrow, M.R. Wootton, R. Moskovic, P.E.J. Flewitt, Fracture behaviour of radiolytically oxidised reactor core graphites: a view, Mater. Sci. Technol. 26 (2010) 899–907, http://dx.doi.org/10.1179/026708309X12526555493477.

[45] M. Mostafavi, S.A. McDonald, P.M. Mummery, T.J. Marrow, Observation and quantification of three-dimensional crack propagation in poly-granular graphite, Eng. Fract. Mech. 110 (2013) 410–420, http://dx.doi.org/10.1016/j.engfracmech.2012.11.023.

[46] M. Mostafavi, N. Baimpas, E. Tarleton, R.C. Atwood, S.A. McDonald, A.M. Korsunsky, et al., Three-dimensional crack observation, quantification and simulation in a quasi-brittle material, Acta Mater. 61 (2013) 6276–6289, http://dx.doi.org/10.1016/j.actamat.2013.07.011.

[47] M.R. Joyce, T.J. Marrow, P. Mummery, B.J. Marsden, Observation of microstructure deformation and damage in nuclear graphite, Eng. Fract. Mech. 75 (2008) 3633–3645, http://dx.doi.org/10.1016/j.engfracmech.2007.11.003.

[48] M. Mostafavi, M.J.J. Schmidt, B.J. Marsden, T.J. Marrow, Fracture behaviour of an anisotropic polygranular graphite (PGA), Mater. Sci. Eng. A 558 (2012) 265–277, http://dx.doi.org/10.1016/j.msea.2012.08.001.

[49] T.H. Becker, T.J. Marrow, R.B. Tait, Damage, crack growth and fracture characteristics of nuclear grade graphite using the double torsion technique, J. Nucl. Mater. 414 (2011) 32–43, http://dx.doi.org/10.1016/j.jnucmat.2011.04.058.

[50] A. Hodgkins, T.J. Marrow, P. Mummery, B. Marsden, A. Fok, X-ray tomography observation of crack propagation in nuclear graphite, Mater. Sci. Technol. 22 (2006) 1045–1051, http://dx.doi.org/10.1179/174328406X114126.

[51] A.G. Evans, High toughness ceramics, Mater. Sci. Eng. A 105–106 (1988) 65–75, http://dx.doi.org/10.1016/0025-5416(88)90481-8.

[52] J. Bohse, Acoustic emission characteristics of micro-failure processes in polymer blends and composites, Compos. Sci. Technol. 60 (2000) 1213–1226.

[53] F. Barthelat, R. Rabiei, Toughness amplification in natural composites, J. Mech. Phys. Solids 59 (2011) 829–840, http://dx.doi.org/10.1016/j.jmps.2011.01.001.

[54] A. Zang, F.C. Wagner, S. Stanchits, C. Janssen, G. Dresen, Fracture process zone in granite, J. Geophys. Res. Solid Earth 105 (2000) 23651–23661.

[55] A. Carrier, J.-L. Got, A. Peltier, V. Ferrazzini, T. Staudacher, P. Kowalski, et al., A damage model for volcanic edifices: implications for edifice strength, magma pressure, and eruptive processes, J. Geophys. Res. Solid Earth 120 (2015) 567–583, http://dx.doi.org/10.1002/2014JB011485.

[56] Z.P. Bazant, Size effect in blunt fracture: concrete, rock, metal, J. Eng. Mech. 110 (1984) 518–535.

[57] M.P. Metcalfe, N. Tzelepi, D. Wilde, Graphite Testing for Nuclear Applications: the Significance of Test Specimen Volume and Geometry and the Statistical Significance of Test Specimen Population, 2014, http://dx.doi.org/10.1520/STP1578-EB. STP 1578. 100 Barr Harbor Drive, PO Box C700, West Conshohocken, PA 19428-2959: ASTM International.

[58] K. McNally, G. Hall, E. Tan, B.J. Marsden, N. Warren, Calibration of dimensional change in finite element models using AGR moderator brick measurements, J. Nucl. Mater. 451 (2014) 179–188, http://dx.doi.org/10.1016/j.jnucmat.2014.03.015.

[59] R. Moskovic, P.E.J. Flewitt, Degradation of graphite in gas cooled reactors due to radiolytic oxidation, Nucl. Eng. Des. 269 (2014) 83–87, http://dx.doi.org/10.1016/j.nucengdes.2013.08.011.

[60] R.K.L. Su, H.H. Chen, S.L. Fok, H. Li, G. Singh, L. Sun, et al., Determination of the tension softening curve of nuclear graphites using the incremental displacement collocation method, Carbon 57 (2013) 65–78, http://dx.doi.org/10.1016/j.carbon.2013.01.033.

[61] G. Del Piero, L. Truskinovsky, Macro- and micro-cracking in one-dimensional elasticity, Int. J. Solids Struct. 38 (2001) 1135–1148, http://dx.doi.org/10.1016/S0020-7683(00)00078-0.

[62] L. Saucedo-Mora, T.J. Marrow, 3D cellular automata finite element method with explicit microstructure: modeling quasi-brittle fracture using meshfree damage propagation, Procedia Mater. Sci. 3 (2014) 1143–1148, http://dx.doi.org/10.1016/j.mspro.2014.06.186.

[63] M. Mostafavi, T.J. Marrow, In situ observation of crack nuclei in poly-granular graphite under ring-on-ring equi-biaxial and flexural loading, Eng. Fract. Mech. 78 (2011) 1756–1770, http://dx.doi.org/10.1016/j.engfracmech.2010.11.004.

[64] A.B. Cook, J. Duff, N. Stevens, S. Lyon, A. Sherry, J. Marrow, Preliminary evaluation of digital image correlation for in-situ observation of low temperature atmospheric-induced chloride stress corrosion cracking in austenitic stainless steels, ECS Trans. 25 (2010) 119–132, http://dx.doi.org/10.1149/1.3407553. Materials Performance Centre, School of Materials, University of Manchester, Manchester, United Kingdom.

[65] B.K. Bay, T.S. Smith, D.P. Fyhrie, M. Saad, Digital volume correlation: three-dimensional strain mapping using X-ray tomography, Exp. Mech. 39 (1999) 217–226.

[66] F. Forsberg, R. Mooser, M. Arnold, E. Hack, P. Wyss, 3D micro-scale deformations of wood in bending: synchrotron radiation muCT data analyzed with digital volume correlation, J. Struct. Biol. 164 (2008) 255–262, http://dx.doi.org/10.1016/j.jsb.2008.08.004.

[67] N. Limodin, J. Réthoré, J.-Y. Buffière, F. Hild, S. Roux, W. Ludwig, et al., Influence of closure on the 3D propagation of fatigue cracks in a nodular cast iron investigated by X-ray tomography and 3D volume correlation, Acta Mater. 58 (2010) 2957–2967, http://dx.doi.org/10.1016/j.actamat.2010.01.024.

[68] M. Mostafavi, D.M. Collins, B. Cai, R. Bradley, R.C. Atwood, C. Reinhard, et al., Yield behavior beneath hardness indentations in ductile metals, measured by three-dimensional computed X-ray tomography and digital volume correlation, Acta Mater. 82 (2015) 468–482, http://dx.doi.org/10.1016/j.actamat.2014.08.046.

[69] T.J. Marrow, A. Steuwer, F. Mohammed, D. Engelberg, M. Sarwar, Measurement of crack bridging stresses in environment-assisted cracking of duplex stainless by synchrotron diffraction, Fatigue Fract. Eng. Mater. Struct. 29 (2006) 464–471, http://dx.doi.org/10.1111/j.1460-2695.2006.01019.x.

[70] P.J. Withers, H.K.D.H. Bhadeshia, Residual stress part 1-measurement techniques, Mater. Sci. Technol. 17 (2001) 355–365.

[71] R. Owen, Neutron and synchrotron measurements of residual strain in TIG welded aluminium alloy 2024, Mater. Sci. Eng. A 346 (2003) 159–167, http://dx.doi.org/10.1016/S0921-5093(02)00547-6.

[72] P.J. Withers, A.P. Clarke, A neutron diffraction study of load partitioning in continuous Ti/SiC composites, Acta Mater. 46 (1998) 6585–6598.

[73] J.J. Biernacki, C.J. Parnham, T.R. Watkins, C.R. Hubbard, J. Bai, Phase-resolved strain measurements in hydrated ordinary portland cement using synchrotron X-rays, J. Am. Ceram. Soc. 89 (2006), http://dx.doi.org/10.1111/j.1551-2916.2006.01118.x, 060612075903006 – ???

[74] E.M. Schulson, I.P. Swainson, T.M. Holden, Internal stress within hardened cement paste induced through thermal mismatch, Cem. Concr. Res. 31 (2001) 1785–1791, http://dx.doi.org/10.1016/S0008-8846(01)00554-3.

[75] S.D. Preston, B.J. Marsden, Changes in the coefficient of thermal expansion in stressed Gilsocarbon graphite, Carbon 44 (2006) 1250–1257, http://dx.doi.org/10.1016/j.carbon.2005.10.045.

[76] M. Mostafavi, T.J. Marrow, Quantitative in situ study of short crack propagation in polygranular graphite by digital image correlation, Fatigue Fract. Eng. Mater. Struct. 35 (2012) 695–707, http://dx.doi.org/10.1111/j.1460-2695.2012.01648.x.

[77] M. Drakopoulos, T. Connolley, C. Reinhard, R. Atwood, O. Magdysyuk, N. Vo, et al., I12: the joint engineering, environment and processing (JEEP) beamline at diamond light source, J. Synchrotron Radiat. 22 (2015), http://dx.doi.org/10.1107/S1600577515003513.

[78] ASTM International, ASTM C565–93(1998), Standard Test Methods for Tension Testing of Carbon and Graphite Mechanical Materials. West Conshohocken, PA, 1999, http://dx.doi.org/10.1520/C0565-93R98.

[79] S. Titarenko, P.J. Withers, A. Yagola, An analytical formula for ring artefact suppression in X-ray tomography, Appl. Math. Lett. 23 (2010) 1489–1495, http://dx.doi.org/10.1016/j.aml.2010.08.022.

[80] O.L. Blakslee, D.G. Proctor, E.J. Seldin, G.B. Spsnce, T. Weng, Elastic constants of compression-annealed pyrolytic graphite, J. Appl. Phys. 41 (1970) 3373–3382.

[81] A.P. Hammersley, S.O. Svensson, M. Hanfland, A.N. Fitch, D. Häusermann, Two-dimensional detector software: from real detector to idealised image or two-theta scan, High Press. Res. 14 (1996) 235–248.

[82] A.M. Korsunsky, K.E. Wells, P.J. Withers, Mapping two-dimensional state of strain using synchroton X-ray diffraction, Scr. Mater. 39 (1998) 1705–1712.

[83] J.R. Santisteban, M.R. Daymond, J.A. James, L. Edwards, ENGIN-X: a third-generation neutron strain scanner, J. Appl. Crystallogr. 39 (2006) 812–825, http://dx.doi.org/10.1107/S0021889806042245.

[84] J.D. Jorgensen, J. Faber Jnr, J.M. Carpenter, R.K. Crawford, J.R. Haumann, R.L. Hitterman, et al., Electronically focused time-of-flight powder diffractometers at the intense pulsed neutron source, J. Appl. Crystallogr. 22 (1989) 321–333, http://dx.doi.org/10.1107/S002188988900289X.

[85] M.R. Daymond, M.W. Johnson, D.S. Sivia, Analysis of neutron diffraction strain measurement data from a round robin sample, J. Strain Analysis Eng. Des. 37 (2002) 73–85, http://dx.doi.org/10.1243/0309324021514844.

[86] A.N. Jones, G.N. Hall, M. Joyce, A. Hodgkins, K. Wen, T.J. Marrow, et al., Microstructural characterisation of nuclear grade graphite, J. Nucl. Mater. 381 (2008) 152–157, http://dx.doi.org/10.1016/j.jnucmat.2008.07.038.

[87] M.R. Joyce, T.J. Marrow, Microstructural scale strain localisation in nuclear

graphite, J. Nucl. Mater. 381 (2008) 171–176, http://dx.doi.org/10.1016/j.jnucmat.2008.07.013.
[88] M. Eto, F.B. Growcock, Effect of oxidizing environment on the strength of H451, PGX and IG-11 graphites, Carbon 21 (1983) 135–147, http://dx.doi.org/10.1016/0008-6223(83)90169-0.
[89] Y. Vertyagina, M. Mostafavi, C. Reinhard, R. Atwood, T.J. Marrow, In situ quantitative three-dimensional characterisation of sub-indentation cracking in polycrystalline alumina, J. Eur. Ceram. Soc. 34 (2014), http://dx.doi.org/10.1016/j.jeurceramsoc.2014.04.002, 3127–3232.
[90] ASTM International, ASTM Username: james.marrow@materials.ox.ac.uk C1161–13, Standard Test Method for Flexural Strength of Advanced Ceramics at Ambient Temperature. West Conshohocken, PA, 2013, http://dx.doi.org/10.1520/C1161.
[91] ASTM International, ASTM C749–92(2002), Standard Test Method for Tensile Stress-Strain of Carbon and Graphite. West Conshohocken, PA, 2013, http://dx.doi.org/10.1520/C0749-92R02.
[92] W.H. Gu, K.T. Faber, Tensile behavior of microcracking SiC-TiB2 composites, J. Am. Ceram. Soc. 78 (1995) 1507–1512.
[93] B. Budiansky, J.W. Hutchinson, J.C. Lambropoulos, Continuum theory of dilatant transformation toughening in ceramics, Int. J. Solids Struct. 19 (1983) 337–355, http://dx.doi.org/10.1016/0020-7683(83)90031-8.
[94] E. Brinksmeier, Improvements in X-ray stress analysis, in: Advances in Surface Treatments. Technology- Applications – Effects, vol. 2, Pergamon Press, 1986, pp. 109–115.
[95] A.J. Wilkinson, G. Meaden, D.J. Dingley, High-resolution elastic strain measurement from electron backscatter diffraction patterns: new levels of sensitivity, Ultramicroscopy 106 (2006) 307–313, http://dx.doi.org/10.1016/j.ultramic.2005.10.001.
[96] S. Björklund, L. Ljung, A review of time-delay estimation techniques, Proc. IEEE Conf. Decis. Control 3 (2003) 2502–2507.
[97] C. Bauer, R. Cramer, J. Schuchhardt, Evaluation of peak-picking algorithms for protein mass spectrometry, Methods Mol. Biol. Clift. NJ 696 (2011) 341–352.
[98] D.M. Collins, M. Mostafavi, R.I. Todd, T. Connolley, A.J. Wilkinson, A synchrotron X-ray diffraction study of in situ biaxial deformation, Acta Mater. 90 (2015) 46–58, http://dx.doi.org/10.1016/j.actamat.2015.02.009.
[99] A.G. Soloviev, E.I. Litvinenko, G.A. Ososkov, A.K. Islamov, A.I. Kuklin, Application of wavelet analysis to data treatment for small-angle neutron scattering. Nuclear instruments and methods in physics research section A: accelerators, spectrometers, Detect. Assoc. Equip. 502 (2003) 500–502, http://dx.doi.org/10.1016/S0168-9002(03)00481-9.